Master thesis and internship[BR]- Master's thesis : Design and analysis of a ducted fan propulsion system for a prototype ultralight aircraft[BR]- Internship

Auteur : Remacle, Colette
Promoteur(s) : Salles, Loïc
Faculté : Faculté des Sciences appliquées
Diplôme : Master en ingénieur civil en aérospatiale, à finalité spécialisée en "aerospace engineering"
Année académique : 2023-2024
URI/URL : http://hdl.handle.net/2268.2/20866

Colette Remacle

Design and analysis of a ducted fan propulsion system for a prototype ultralight aircraft

Master thesis submitted in partial fulfillment of the requirements for the degree of Master in Aerospace Engineering

University of Liege
Faculty of Applied Sciences
Academic Year 2023-2024

Abstract

This thesis focuses on the design and analysis of a ducted fan propulsion system for the Mindus Belvedere ultralight aircraft. The aim is to design the rotor and stator of the ducted fan system according to specific aerodynamic performance requirements and to analyze the aerodynamic behavior of the system during cruise flight using Computational Fluid Dynamics (CFD).

The design phase involved the use of a reversed Blade Element Method (BEM) to determine the rotor and stator configurations, with a comparison of two airfoils, NACA 2412 and NACA 65-210. The NACA 65-210 was ultimately selected. The design was validated by a performance analysis, made using a BEM implemented in MATLAB and the DFDC (Ducted Fan Design Code) software. The analysis confirmed that the selected airfoil provides optimal thrust and efficiency, with good performance across varying operational conditions.

A CFD study was then conducted using an actuator disk to simulate the rotor, first in axisymmetry and then in two dimensions. The axisymmetric analysis revealed that the duct contributed with additional thrust at the design point. A more accurate representation of the thrust performances of the rotor could be made, using a more realistic axial velocity inside the duct than in the design phase. The analysis also highlighted how this axial velocity differed from the flight velocity, especially at low speeds and low collective pitch angles, affecting overall performance. The contribution of the duct to the thrust could be computed and appeared to be positive at lower flight velocity and negative at higher flight velocity.

Additionally, the two-dimensional analysis revealed significant variations in velocity and mass flow in the upper and lower part of the duct. A zone of turbulence and a zone of zero-magnitude velocity was found in the lower part of the duct. This flow distortion could lead to negative impact on the engine performance and structural problems.

Keywords: Ultralight Aircraft, Ducted Fan Propulsion, Actuator Disk Modeling, Blade Element Method, Computational Fluid Dynamics

Acknowledgment

First and foremost, I would like to express my gratitude to Gaël Minne for giving me the opportunity to work on his ULM project. His trust and confidence in me were the starting points for this great journey.

I am also thankful to my advisor, Professor Loïc Salles, for his invaluable guidance and insightful feedback throughout this project. His expertise and unwavering support were key factors in helping me navigate the challenges of this research.

Additionally, I would like to extend my heartfelt appreciation to Professor Koen Hillewaert, whose expertise and assistance were crucial in performing this thesis. His willingness to share his knowledge and provide detailed guidance greatly enriched my work.

Special thanks go to Mario and Charles, who shared the same office and were a source of camaraderie and support throughout this journey. Your presence and discussions made the work environment more enjoyable and productive.

To all my friends and particularly, Lucas, whose support all the way from Chile was a constant source of motivation, and Oscar, who was there for me every day with words of encouragement — thank you both for being pillars of support during this journey.

I am deeply grateful to my family for their unwavering belief in me. My brother, for his valuable advice; my father, for meticulously reviewing my work and offering corrections; and my mother, for her endless emotional support, which kept me grounded and focused.

Lastly, I want to thank my boyfriend, Simon for his daily support and encouragement during the entire semester, until the very end, even from afar in Seoul. Your patience and love have been a source of strength throughout this process.

Contents

List of Figures

List of Tables

Chapter 1

Introduction

1.1 Context and motivations

In the context of a world with limited resources, ultralight aircraft could be the future of recreational aviation. Having a lower mass and being more efficient allows them to burn less fuel in comparison with a typical single engine piston like the Cessna 172 Skyhawk, the most produced aircraft of all time [25].

The 12th Sustainable Development Goal (SDG) [10] of the European Union focuses on ensuring sustainable consumption and production patterns, which is crucial for promoting economic growth while minimizing environmental impacts. This goal emphasizes the need for innovative solutions in various industries, including aviation, to enhance resource efficiency and reduce waste. Aligning with this objective, the Mindus concept-plane represents a meaningful step towards a more sustainable and efficient aviation sector. Through advanced technologies and a design that is both cutting-edge and efficient, the Mindus Belvedere aims to reduce fuel consumption thereby contributing to the EU's broader sustainability targets.

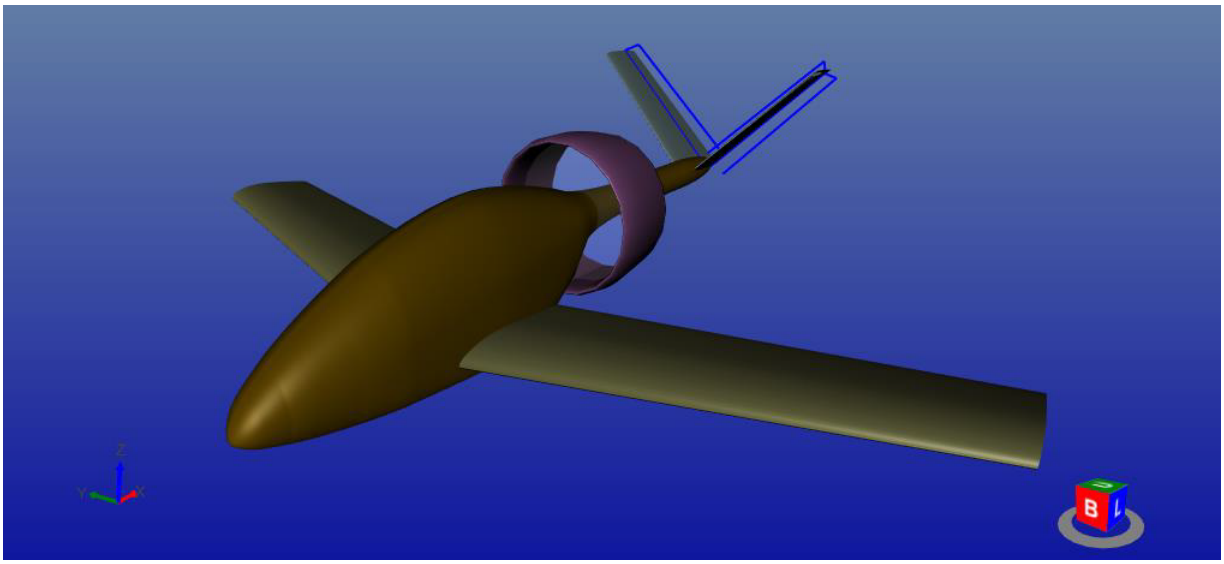

Figure 1.1 - *CAD of the Mindus Belvedere aircraft.*

.

The focus of this master's thesis is an innovative concept-plane named Belvedere and created by the company Mindus. It has been designed with the primary occupant's flight experience at its core. The aircraft is intended to recede into the background, allowing the pilot to fully engage in the activities it enables, such as exploring the overflown area, enjoying a sporty evolution in the air mass, and experiencing the controlled sensations of the joy of flying and being "in command" of the moment. The Mindus Belvedere serves as a tool for enhancing techniques through applied research, creating an immersive flight experience where the occupant is an integral part of the journey. The engine has been chosen to be behind the cockpit as it allows to have a clear, 270° view on the outside.

Targeting a diverse audience, the Mindus concept-plane serves several groups. Firstly, it attracts the discovery-based tourism market, offering unique adventures for tourists seeking picturesque flights or specific sightseeing experiences. Secondly, ultralight motorized aircraft (ULM) operators, including those at ultralight airfields, can benefit from the advanced techniques and features integrated into this design. Finally, amateur pilots seeking an aircraft that balances performance, safety and aesthetics will appreciate the innovative qualities of this concept-ULM.

The qualities of the Mindus aircraft further enhance its appeal. With maximized visibility in all forward orientations, pilots can confidently navigate their flights. The enhanced seat comfort and ergonomics ensure a pleasant experience during long journeys. Fuel efficiency contributes to economical flight hours and a reduced fuel consumption, while stringent safety features prioritize the pilot's well-being. The attractive aesthetics of the concept-plane makes it visually appealing, and energy optimization aligns with sustainability goals. Noise reduction measures minimize disturbances, and an embedded digital recording system captures and preserves flight memories in a digital format.

The design of the concept-plane can be seen in the Figure 1.1 and the main characteristics of this aircraft are the following:

- ULM tandem two-seater (VFR-only);
- retractable tricycle landing gear;
- mid-mounted ducted fan propulsion;
- proven Rotax engine (max 108 hp);
- V-tail design;
- highly inclined forward passenger/pilot seating position;
- cockpit/canopy widely open in all directions, non-pressurized;
- unobstructed view (instruments and controls relocated);
- climate-controlled cabin with IR and UV protection canopy.

A conceptual design of the ULM has been performed by the company OAD in 2020. The main features of the aircraft are summarized in the Table 1.1.

Table 1.1 - *Main specifications of the Mindus Belvedere aircraft.*

Specification	**Description**
Type	UltraLight Motorized Aircraft (ULM)
Engine	Ducted fan alimented by a Rotax 912-ULS
Power	94 HP
Wingspan	7.98 m
Length [1]	6.59 m
Height [2]	2.54 m
Maximum Takeoff Weight (MTOW)	531 kg
Range [3]	879 km
Cruise speed	252 km/h
Cruise altitude	2400 m
Seating capacity	2 (including pilot)

The propulsive equipment of the Mindus Belvedere is a ducted fan system (DFS) placed around the fuselage as shown in Figure 1.2. The DFS is composed of a rotor and a stator placed in the center of the duct. The design and the aerodynamic study of the DFS will be the center of this master thesis.

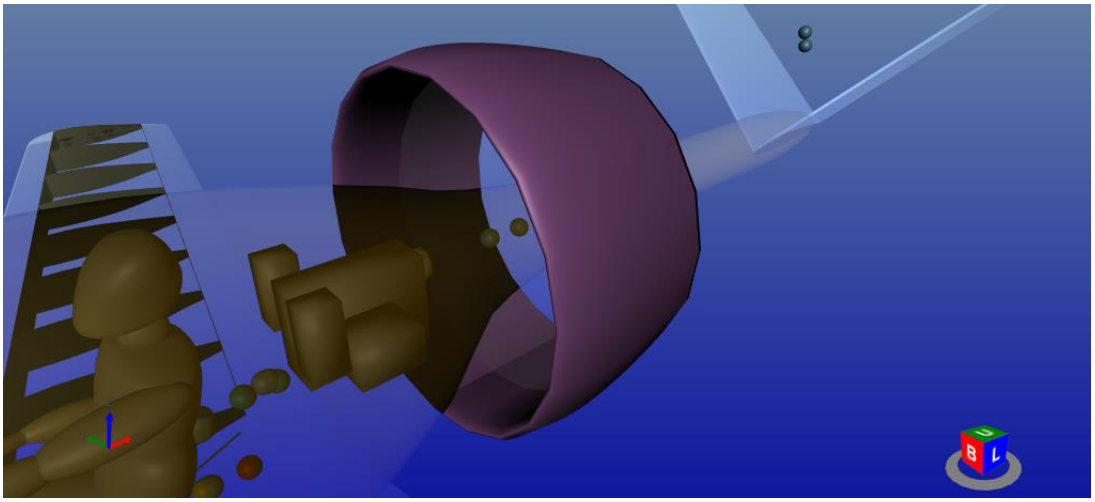

Figure 1.2 - *The ducted fan system of the ULM.*

In this introduction, the state of the art will be developed, from the definition of an ultralight aircraft and a ducted fan to the overview of similar airplanes in use. After, the thesis outline and objectives will be described.

[1] The length of the aircraft from nose to tail.
[2] The height of the aircraft from the ground to the highest point.
[3] The maximum distance the aircraft can fly without refueling.

1.2 State of the art

The definition of an ultralight motorized aircraft will be given with an example. Then the concept of ducted fan will be defined, followed by a presentation of its advantages and drawbacks and its use in the aeronautical industry. Finally, an overview will be made on past and actual similar aircraft.

1.2.1 UltraLight Motorized Aircraft

An ultralight motorized aircraft (ULM) is a category of lightweight aviation vehicles designed for recreational use. According to the European Aviation Safety Agency (EASA) regulations, as written in the EASA Basic Regulation (EU) 2018/1139 [11], an ultralight aircraft is defined by a specific weight and performance criteria. However, regulations may vary slightly between countries. In France, the aviation authority aligns with European standards but specifies that the Maximum Take Off Weight (MTOW) for an ultralight aircraft must not exceed 330 kg if the aircraft is equipped with a single seat or 345 kg if equipped with parachute. For two-seaters, the MTOW is 500 kg or 525 kg with parachute and 545 kg if it operates over water. Additionally, the aircraft must not exceed a stall speed of 70 km/h (37.8 knots) and must be limited to a maximum of two seats.

An example of a popular ultralight aircraft in Europe is the Comco Ikarus C42 shown in Figure 1.3.

Figure 1.3 - *Comco Ikarus C42 [14].*

The Comco Ikarus C42 has a high-wing design and tricycle landing gear. It is constructed using a combination of composite materials and fabric-covered metal tubing. The C42 typically uses a Rotax 912 engine, available in 80 hp or 100 hp variants, with a cruising speed of up to 180 km/h [13]. It has a cockpit with side-by-side seating for two and includes basic instrumentation suitable for visual flight rules (VFR), it is a common choice for both recreational pilots and flight training in Europe [9].

1.2.2 Ducted fan engine

After the definition of the concept of ULM, the engine type ducted fan will be defined, and its characteristics will be listed. Some examples will be given.

Definition of a ducted fan engine

To begin, the characteristics and functionality of the ducted fan engine will be explored. Over time, various definitions have been proposed. In its most basic form, a ducted fan is a fan or propeller enclosed within an annular wing or shroud. However, the need for a more precise definition becomes evident when considering related technologies like turbofans and propfans, which also involve enclosed fans.

According to van den Dungen [32], the primary distinction between these engine types lies in their performance and operating conditions. Turbofans are generally preferred for high-speed applications, while propfans or ducted fans are more suitable for low-speed, high-efficiency applications. Raymer [28] notes that propellers, including those in propfans, offer higher propulsive efficiency than turbofans because they move a larger mass of air at a lower velocity, consuming less fuel in the process. Unlike propfans, ducted fans lack an engine core that further accelerates the airflow, similar to how a turbofan does. Consequently, the performance characteristics of ducted fans are closer to those of turboprops (which are not ducted), offering a high bypass ratio and low fuel consumption during cruise.

History of ducted fan

The first work made on ducted propellers was published in 1931 in Italy, by Luigi Stipa. Due to its wind tunnel experiments, it has been able to show the benefits of ducting a propeller for the static operation and low speed flight [30]. L. Stipa theorized that directing propeller thrust through a tapered venturi tube would increase thrust efficiency and stability, reduce noise, and eliminate propeller tip vortices. In 1932, he designed his airplane called Stipa-Caproni which demonstrated a good stability and lift at low speed but had a top speed of 81 mph (130 km/h) due to the induced drag [19].

Since the early experiments in the 1930s, interest in the ducted propeller has grown significantly, especially now that hovering flight and vertical take-off have become practical and achievable. The ducted fan can find applications in diverse aircraft as autogyros, compound helicopters, seaplanes, short takeoff aircraft, vertical takeoff aircraft ... An example of aircraft using a ducted fan is shown on Figure 1.4.

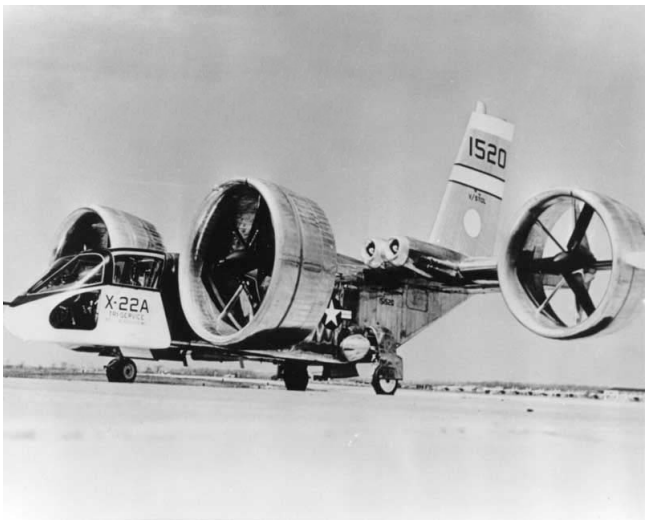

Figure 1.4 - *Bell X-22 (1962) [34].*

The Bell X-22 has been developed during a research program focusing on vertical take-off and landing (VTOL) aircraft. This aircraft is equipped with four ducted fan systems (DFS) that can rotate 90 degrees, allowing them to be utilized for both forward flight and VTOL capabilities [27] [32].

Advantages and drawbacks of a DFS

The use of a ducted fan can be justified by several points which will be developed hereafter. Excepted if another source is specified, the main explanation and justification presented hereafter is based on the work of M De Piolenc and G. Wright presented in the book Ducted Fan Design [27].

In cruising flight, an open propeller is immersed in a stream of fluid, creating three distinct regions: the inflow into the propeller, the slipstream behind it, and the free stream that bypasses the propeller. Propeller design calculations typically focus on these conditions. However, during takeoff, when the aircraft is at rest or moving slowly, the dynamics change significantly. The propeller is then in a static air mass, resulting in only two regions: the slipstream and the inflow region, as can be seen in Figure 1.5. This setup can lead to a region of reversed flow near the propeller tips, reducing the effective disk area and limiting the airflow through the propeller when maximum mass flow is needed.

Surrounding the propeller with a close-fitting shroud or duct can drastically change this scenario. The duct creates a solid boundary that simplifies the airflow's path, ensuring that air particles flow smoothly around the duct's leading edge, as can be observed in the Figure 1.6. This setup prevents the reversed flow issue and allows the propeller to carry a load across its entire span, including the tips. The duct also helps maintain a more consistent airflow direction, similar to the conditions experienced during cruising. This configuration enhances the propeller's efficiency and overall performance, especially during critical phases like takeoff.

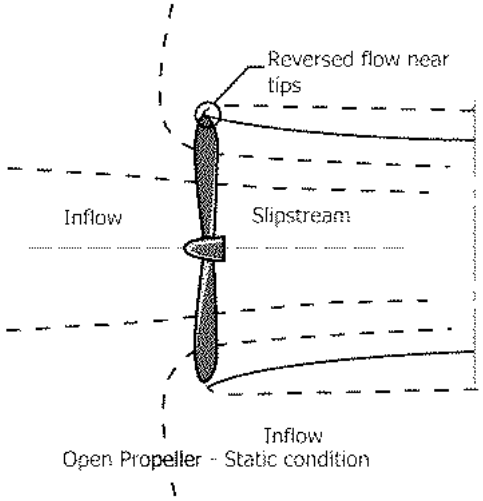

Figure 1.5 - *Open propeller - Static condition [27].*

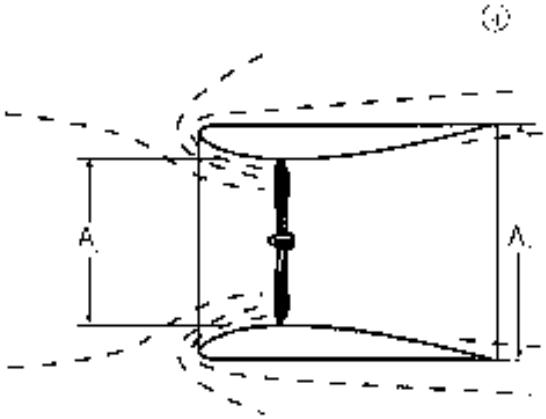

Figure 1.6 - *Ducted propeller - Static condition [27].*

The effects induced by the previous explanation are listed hereafter.

(a) The propeller inside of the duct operates nearer to its ideal operating along the aircraft's speed range, which allows fewer design compromises.

(b) The effective diameter of the ducted propeller is larger than its physical diameter. In fact, the slipstream contracts behind an open propeller at cruise while the slipstream diameter of the ducted fan is that of the duct exit. However, a larger diameter represents a smaller velocity increment and a larger mass flow. It means a higher thrust and horsepower.

(c) While the propeller develops about the same thrust as before, an additional force acts on the duct. This force arises from the aerodynamic interactions between the duct and the airflow around it. When the duct is correctly shaped, it harnesses these interactions to create extra thrust because the duct creates a suction peak near its leading edge, generating additional forward thrust [7]. Consequently, the overall efficiency of the propulsion system is enhanced, making the design more effective than a traditional open propeller system.

(d) During the cruise, the effective area of the fan is approximately that of the duct inlet, which is larger than the swept area of the propeller itself.

(e) It allows noise suppression three different ways.

- Operating the propeller within its optimal flow and load parameters eliminates the "buzz" noise typically generated by propeller tips, a common source of noise in propeller-driven aircraft.
- Surrounding the propeller with a duct allows for the incorporation of acoustic treatments, which can absorb noise before it reaches surrounding areas.
- Ducted fans enhance static and low-speed thrust, enabling steeper climb angles during takeoff, which in turn reduces the noise experienced at the airport boundary.

(f) It provides a higher ground safety, avoiding an open air propeller reduces the risk of an accident in the ground. This is most of all important in the case of recreational aviation where non-pilot can go near the airplane.

Even if there are a lot of advantages of having a ducted fan, there are also downsides, indeed, positive sides occur mostly at low velocity or at cruise. For example, at higher flight velocity, the duct inlet shape causes losses in the propulsive efficiency, the duct produces some additional thrust mostly in the lower range of the flight velocity of the airplane, in the higher range it can create some drag [7]. Furthermore, the contraction of the slipstream of the open propeller tent to reduce at high velocity, which reduces the difference of mass flow between an open and a closed propeller [7]. Finally, without acoustic treatment, the interaction between the fan and the inner side of the duct might cause an increase in noise. The global noise emission must thus be studied carefully [15].

1.2.3 Similar airplanes

Two interesting cases of small airplanes having a ducted fan are presented hereafter. The first one is the Fan Jet 600, shown in Figure 1.7 and the second one is the XAZ-1 Marvelette, shown in Figure 1.8.

Figure 1.7 - *Fan Jet 600 [6].*

Figure 1.8 - *XAZ-1 Marvelette [1].*

The Fan Jet 600 is an advanced training aircraft featuring a ducted fan propulsion system powered by an Allison 250-C30 turboshaft engine, delivering 650 shaft horsepower. This configuration offers reduced fuel consumption and noise compared to traditional jets. The aircraft can achieve a maximum speed of 275 knots indicated airspeed (kias) (509 km/h) and a cruise speed of 200 knots true airspeed (370 km/h). It has a range of 750 nautical miles (1,389 km) and a service ceiling of 25,000 feet (7,620 m). The maximum takeoff weight (MTOW) is 2300 kg [6].

Primarily designed for military pilot training, the Fan Jet 600 provides a realistic jet-like experience, making it ideal for transitioning pilots from basic to advanced jet training. It is also showcased in airshows and demonstration flights, highlighting its versatile capabilities. The aircraft's modern cockpit instrumentation and controls offer a comprehensive training environment. Its ducted fan system enhances performance and safety by ensuring smooth airflow.

The XAZ-1 Marvelette was an experimental research aircraft developed by Mississippi State University in the early 1960s. It was designed to investigate boundary layer control systems, utilizing a variable camber wing constructed from glass fiber, featuring a perforated surface and suction pumps. The aircraft was a modified version of the Anderson Greenwood AG-14, transformed by the Parsons Corporation and equipped with a ducted fan propulsion system [27].

This aircraft had a maximum takeoff weight (MTOW) of 2,000 lb (907 kg). It was powered by a Continental C-90-12 air-cooled flat-four engine, producing 95 hp (71 kW), and equipped with a 3-bladed variable-pitch ducted fan propeller with a diameter of 5 ft 6 in (1.68 m). The aircraft was designed to accommodate a crew of two and had a wingspan of 26 ft 2 in (7.98 m).

This airplane is interesting because, as specified before, it has been used in order to make some research about the Boundary Layer Ingestion (BLI). The BLI involves integrating the propulsion system within the aircraft's airframe to ingest part of the low-momentum region from the boundary layer as inlet of the engine, thereby reducing wake and the growth of the boundary layer along the airframe. As demonstrated in various papers [29], the BLI is promising in the context of electric ducted fans as it could improve significantly the aerodynamic coefficients, eliminate flow separation and delay in onset of the stall phenomenon.

1.3 Thesis outline and objectives

Initially, the objective of the thesis was to make a Computational Fluid Dynamic (CFD) study of the entire Mindus concept-plane at different flight phases. However, as the rotor and the stator were not yet designed in the conceptual design of the ULM, the objectives had to be adapted. The first objective is thus to make the design of the rotor and of the stator and be able to simulate the performances at different flight velocities. And the second objective is to make the computational fluid dynamic study but reduced to the cruise phase of flight and the front part of the ULM.

This work will be separated in two main parts.

- The design part, which consists in the design of the rotor and the stator. This will be performed using a reversed blade element method based on the required thrust and an approximation on the mass flow. The method will be explained, focusing on the velocity triangles and the generated forces at the blade. Then the obtained design will be described and analyzed for two different airfoils, the NACA 2412 and the NACA 65-210. One of the two airfoils will be chosen, and a performance analysis will be made, using a blade element method slightly adapted to ducted propeller and then using DFDC software.
- The computational fluid dynamics part, which has the objective to test the designed rotor with the duct. The focus of this section will be the inlet of the rotor, as the rear part and the v-tail will not be considered. To do so, the actuator disk method will be used to simulate the rotor in Ansys Fluent software. The effects of the duct will be studied in three dimensions with axisymmetry, using the upper part of the cockpit and in two dimensions to consider the lower part as well. The focus will be on the velocity profile inside of the duct, the thrust generated by the duct and the performances of the rotor.

Chapter 2

Design of the rotor and the stator

In this chapter, the objective will be to make the design of the rotor and the stator of the ducted fan. To do so, the theoretical background will be developed, mostly describing the design method. Then the method will be applied to two different airfoils, the NACA 2412 and the NACA 65-210 and the obtained design will be shown, one of the two airfoils will be selected. Finally, the performance charts will be computed and analyzed.

2.1 Theoretical background

Inside of the duct, the stator is placed after the rotor. While the main goal of the rotor is to generate thrust, the goal of the stator is to redirect the flow axially. Indeed, after the rotor, the flow has a swirl motion that will be canceled by the stator. In the case of this ULM the stator is also needed to sustain the duct.

2.1.1 Introduction and hypotheses of the BEM

This section recalls the mathematical derivation of the blade element method. The main development is based on the course notes from K. Hillewaert (2023) [17] and adapted to a ducted propeller.

The Blade Element Method (BEM) is a numerical technique used to analyze and design rotor blades for wind turbines, helicopters and propellers. It considers variations in flow conditions along the radius of the propeller by applying principles of mass, momentum, and energy conservation in stream tubes between two infinitely close stream surfaces. The method involves dividing the blade into small segments, or "blade elements", and calculating the aerodynamic forces on each element using airfoil polars. These infinitesimal contributions are then integrated to determine the total thrust produced, as well as the torque and power consumed by the propeller. BEM is also used for preliminary design, offering a computationally efficient way to estimate blade performance.

The design of the rotor and the stator will be performed using a reversed BEM. Usually, the BEM is used in order to approximate the performances of an already designed blade. Hereafter, the blades will be designed to match the required performances.

The hypotheses of the method are presented below.

- Independence of the blade elements. The forces and the flow conditions on one element are considered to not affect the neighboring elements.
- Quasi-steady flow. The aerodynamic forces are considered to change slowly enough to be approximated as steady at each instant.
- Two-dimensional flow. The tip vortices and spanwise flow are neglected.
- Uniform inflow. The flow is considered to enter the rotor axially at every radial station.
- Inviscid and incompressible flow.
- No interaction between the blades. The aerodynamic interference from other blades is neglected.

The objective of the BEM here will be to determine the required chord and torsional angle of the blade at each radius along the span, to produce the required thrust. To do so, the velocity component must be determined at some axial position inside of the duct and the forces at the rotor and at the stator must be computed along the blades at each radial blade element.

2.1.2 General concept

In order to describe the velocity inside of the duct, five triangles of velocity will be used, as can be seen in Figure 2.1. Each velocity triangle has three components, the absolute velocity $\mathbf{v}$ in blue, the tangential velocity $\mathbf{u}$ in green and the relative velocity $\mathbf{w}$ in red. Those three velocities are related by the equation:

$$\mathbf{v} = \mathbf{w} + \mathbf{u}. \tag{2.1}$$

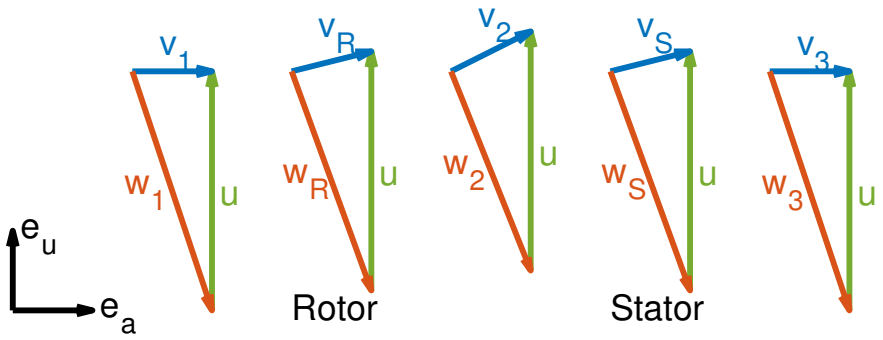

Figure 2.1 - *Velocity triangles inside of the duct.*

Each velocity can be divided in its component in the axial and in the tangential direction, respectively denoted with $\{.\}_a$ and $\{.\}_u$. In each triangle the relation between the components is:

$$\begin{cases} \mathbf{v} = v_a\mathbf{e}_a + v_u\mathbf{e}_u \\ \mathbf{w} = w_a\mathbf{e}_a + w_u\mathbf{e}_u = v_a\mathbf{e}_a + (v_u - u)\mathbf{e}_u. \end{cases} \tag{2.2}$$

The velocities before and at the rotor will be denoted respectively with $\{.\}_1$ and $\{.\}_R$, the velocities between the rotor and the stator $\{.\}_2$ and the velocities at and after the stator will be noted with $\{.\}_S$ and $\{.\}_3$.

From the velocity triangle and the aerodynamic properties of the blades, the resulting forces will be computed. Each blade is divided into smaller cross sections of area and mass flow passing through of:

$$dA = 2\pi r dr, \qquad d\dot{m} = \rho dA v_a. \tag{2.3}$$

The contribution dF represents the force exerted on the blade in the entire stream tube so that it is the sum of the forces on all the blades. The components of this force will be considered as positive if oriented along the positive axial and tangential direction. The force dF can be decomposed following the aerodynamics components, the drag dD and the lift dL or following the axial and tangential component, respectively dF_a and dF_u. The relation between those forces will be used to determine the stagger angle and the chord length required at each radial station to generate the thrust.

The decomposition of the force increment dF in its axial and tangential is directly linked to the thrust and torque increment, dT and dC as:

$$dT = -dF_a, \qquad dC = r dF_u. \tag{2.4}$$

2.1.3 Velocity triangles

Now that the concept of the triangle and the general relation between its components has been defined, the component and angle of each triangle will be computed.

- Constant components in all the triangles.
  - The tangential velocity $\mathbf{u}$. It is computed using the blade rotation speed Ω in [rad/s] of the rotor and is directly proportional to the radius r in [m] as:

    $$u(r) = \Omega r. \tag{2.5}$$

  - The axial component of the absolute velocity, v_a, is considered to be constant inside of the duct. Also, before the rotor, v_1 is purely axial due to the hypothesis previously made on the air entering the rotor. The velocity v_3 is also considered to be purely axial because it is located after the stator that has the objective to redirect the velocity axially.

    The absolute velocity v_1 can be deduced from the mass flow as:

    $$v_a = v_1 = \frac{\dot{m}}{\rho\pi(r_t^2 - r_h^2)}, \tag{2.6}$$

    with r_t the radius at the tip of the blades and r_h the radius at the hub of the blades.

- Absolute velocity of each velocity triangle.
  - The tangential component of the absolute velocity after the rotor, v_{u2} is chosen according to the whirl distribution which is chosen to be a free vortex distribution [8]. The velocity v_{u2} is thus defined as:

    $$v_{u2} = \frac{\Delta h^0}{u} \propto \frac{C}{r}. \tag{2.7}$$

- The tangential components of v_R and v_S are computed making the average of the upstream and downstream conditions of each one:

$$\begin{cases} v_{uR} = \dfrac{v_{u1} + v_{u2}}{2} = \dfrac{v_{u2}}{2} \\ v_{uS} = \dfrac{v_{u2} + v_{u3}}{2} = \dfrac{v_{u2}}{2} \end{cases} \tag{2.8}$$

  with $v_{u1} = 0 = v_{u3}$ due to the presence of the stator.

- Velocity and angle at the rotor.

  - The relative flow angle of the rotor, denoted as β_R is defined as:

$$\beta_R = \arctan \frac{v_{uR} - u}{v_a} \tag{2.9}$$

    with β_R that will always be considered negative in this method.
  - The relative velocity of the rotor w_R is:

$$w_R = \sqrt{v_a^2 + (v_{uR} - u)^2}. \tag{2.10}$$

- Velocity and angle at the stator.

  - The absolute flow angle of the stator, denoted α_S is computed as:

$$\alpha_S = \arctan \frac{v_{uS}}{v_a}. \tag{2.11}$$

  - The absolute velocity at the stator is:

$$v_S = \sqrt{v_{uS}^2 + v_a^2}. \tag{2.12}$$

2.1.4 Generated forces

After the determination of the velocity triangles at each radial station, the forces at the rotor and at the stator can be computed along the span. The representation of the forces vector at the rotor and at the stator can be observed in Fig. 2.2 and Fig. 2.3. In those two diagrams, only the directions of the vectors are important, their magnitudes had been adapted for the clarity of the diagrams.

In Fig. 2.2 and Fig. 2.3, the force increment dF is represented with a black arrow. The forces in purple represent the axial and the tangential component of dF, respectively dF_a and dF_u. The forces in yellow represent the lift and the drag increment at the blade, denoted dL and dD. The drag at the rotor is aligned with w_R and the drag at the stator is aligned with v_s. The stagger angle χ represents the angle between the blade chord and the tangential direction. The angle of attack aoa is the angle between the blade chord and the coming flow seen by the blade.

The detailed computation of each force increment is presented hereafter.

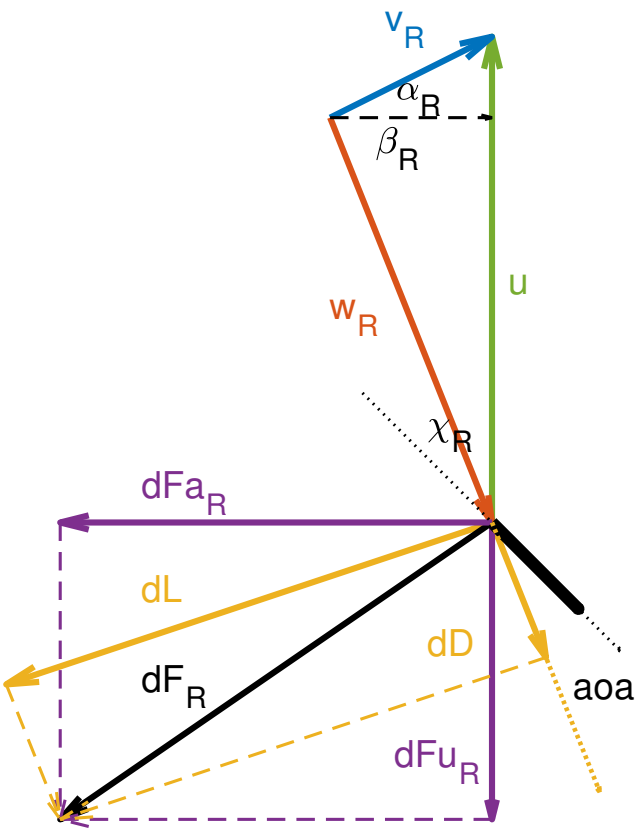

Figure 2.2 - *Diagram of the forces at the rotor.*

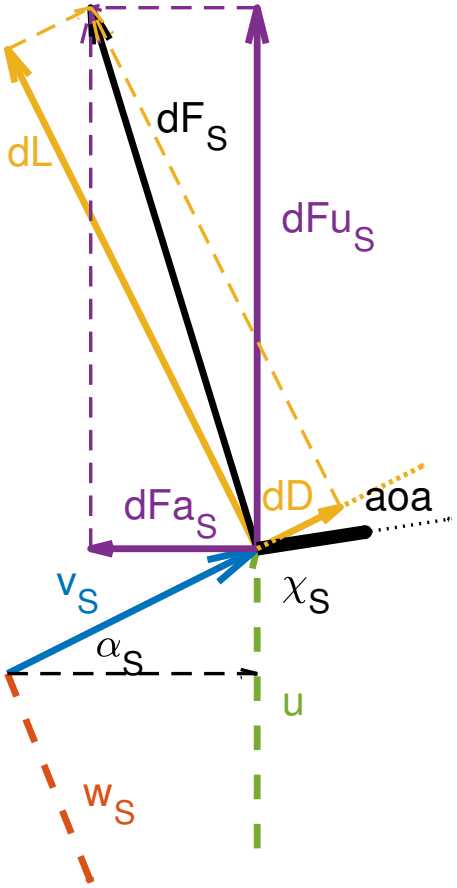

Figure 2.3 - *Diagram of the forces at the stator.*

- At the rotor: the increment of the force dF_R, oriented in the tangential direction, can be computed as:

$$dF_{u_R} = -d\dot{m}(v_{u2} - v_{u1}) = -d\dot{m}v_{u2}. \tag{2.13}$$

The lift and drag increments by chord unit, respectively denoted as $dL_{/c}$ and $dD_{/c}$, are computed as:

$$dL_{/c} = C_L n_R \frac{1}{2}\rho w_R^2 dr, \qquad dD_{/c} = dL_{/c}\tan(\epsilon). \tag{2.14}$$

with n_R the number of rotor blades and ϵ the glide angle of the airfoil, computed as $\epsilon = \arctan\frac{C_D}{C_L}$.

The chord at each radius of the rotor, denoted c_R, can be deduced from the relation between the components of the force increment dF_R:

$$dF_{uR} = -dL_{/c}c_R(\cos(\beta_R) - \tan(\epsilon)\sin(\beta_R)). \tag{2.15}$$

Knowing the chord c_R, the axial component of the force increment can be computed:

$$dF_{aR} = +dL_{/c}c_R(\sin(\beta_R) + \tan(\epsilon)\cos(\beta_R)). \tag{2.16}$$

From the axial component of the force, the pressure difference at the rotor is computed:

$$\Delta p_R = -\frac{dF_{aR}}{dA}. \tag{2.17}$$

- At the stator, the same principle is applied. The increment of the force dF_S oriented in the tangential direction is chosen to result in a zero component of the absolute velocity in the tangential direction ($v_{u3} = 0$) so that:

$$dF_{u_S} = -dF_{u_R} = d\dot{m}v_{u2}. \tag{2.18}$$

The lift and drag by unit of chord are computed as in Eq. 2.14 but using the absolute velocity v_S and the number of stator blades n_S:

$$dL_{/c} = C_L n_S \frac{1}{2}\rho v_S^2 dr, \qquad dD_{/c} = dL_{/c}\tan(\epsilon). \tag{2.19}$$

The axial and tangential projection of the force are:

$$dF_{uS} = dL_{/c}c_S(\cos(\alpha_S) + \tan(\epsilon)\sin(\alpha_S)), \tag{2.20}$$

$$dF_{aS} = dL_{/c}c_S(\sin(\alpha_S) - \tan(\epsilon)\cos(\alpha_S)). \tag{2.21}$$

The pressure difference is then deduced using the axial force:

$$\Delta p_S = \frac{dF_{aS}}{dA}. \tag{2.22}$$

The total pressure difference is then the sum of the delta pressure at the rotor and at the stator:

$$\Delta p = \Delta p_S + \Delta p_R. \tag{2.23}$$

The stagger angle χ is the angle between the rotational plane of the rotor or the stator and the blade. The relation between χ and the angle of attack can be can be deduced from Fig. 2.2 and Fig. 2.3 and computed from the above parameters, at the rotor, as:

$$\chi_R = \frac{\pi}{2} + \beta_R + aoa. \tag{2.24}$$

And for the stator:

$$\chi_S = \frac{\pi}{2} - \alpha_s + aoa. \tag{2.25}$$

2.2 Setup and initialization of the method

In this section, the setup of the method will be explained. First, two airfoils will be chosen, then the mass flow and the required work will be approximated, all the parameters necessary for the initialization will be explained and finally, the loss will be evaluated.

2.2.1 Choice of the airfoil polar

To choose the appropriate airfoil, the Reynolds number is approximated using the formula:

$$Re = \frac{\rho w_R c_0}{\mu} \tag{2.26}$$

with

- c_0 in [m] a first estimation of the chord, obtained neglecting the drag in equation (2.15) so that $dF_{uR} = dL\cos(\beta_R)$;
- ρ the air density at cruise in [kg/m^3];
- μ the dynamic viscosity at cruise in [kg/(m/s)].

The obtained Reynolds number is 1.6×10^5. With the Re, two airfoils are selected, the NACA 2412 and the NACA 65-210. The NACA 2412 is a popular airfoil which can be used at low Reynolds number. It is a common airfoil for small aircraft and has stable and predictable aerodynamic characteristics [24] [3]. The NACA 65-210 is part of the NACA 6-series and is optimized for achieving favorable pressure distributions and reducing drag. It has efficient cruise performance [20] [2]. The airfoil polars are generated using XFOIL. They allow to choose the glide angle ϵ and the lift coefficient for the design point. For the NACA 65-210, the maximum lift-to-drag coefficient $\frac{C_L}{C_D}$ is 58.98 and occurs at an angle of attack (aoa) of 3.5°, the related lift coefficient is 0.58 which is under the maximum lift authorized, defined as $0.75 \times C_{Lmax}$ to avoid stall on the blades. The NACA 2412 has its maximum $\frac{C_L}{C_D}$ of 66.6 for an aoa of 6° and a related lift coefficient of 0.89. The characteristics of each airfoil are summarized in Table 2.1 and the polars are shown in the Appendix A.

Table 2.1 - *Characteristics of the design point for the NACA 65-210 and the NACA 2412.*

	$\frac{C_L}{C_D}$	C_L	aoa
NACA 65-210	58.98	0.58	3.5°
NACA 2412	66.6	0.89	6°

2.2.2 Approximation on the mass flow

The mass flow on cruise is approximated using the fan swept area as the capture area A_0:

$$\dot{m} = \rho A_0 v_\infty \tag{2.27}$$

with

- A_0 the rotor swept area in [m^2] computed as $A_0 = \pi(r_t^2 - r_h^2)$;
- ρ the air density at cruise in [kg/m^3];
- v_∞ the velocity of the airplane on cruise in [m/s].

When designing the rotor and the stator of the ULM, an assumption must be made on the axial velocity inside of the duct, v_1. It will here be assumed that v_1 is equal to the velocity of the airplane on cruise, and thus that the fan swept area is the capture area as stated before. Later a CFD study will be performed and the difference between the axial velocity inside of the duct and the velocity of the airplane will be studied in more details.

2.2.3 Evaluation of the work

The design will be made based on the required thrust and on the mass flow at cruise. Now that the mass flow has been approximated, the thrust must be translated to a required work Δh^0, done by the rotor and the stator which corresponds to the total enthalpy change over the disk [17].

The equation of Δh^0 in the farfield conditions is:

$$\Delta h^0 = \frac{v_j^2 - v_\infty^2}{2} + \frac{\Delta p}{\rho} + \Delta\epsilon \tag{2.28}$$

with

- the jet velocity v_j computed using the required thrust:

$$T = \dot{m}\Delta v = \dot{m}(v_j - v_\infty) \tag{2.29}$$

- $\frac{\Delta p}{\rho}$ the static pressure difference which is equal to 0 in the farfield as it is equal to the atmospheric pressure,
- the change of internal energy $\Delta\epsilon$, that is equal to the losses due to the friction and the swirl.

In order to evaluate the work Δh^o, the losses will be approximated to be zero at first and with the resulted pressure difference computed using Eq. (2.23), the losses ξ due to the fact that the efficiency of the stage is different to 1 can be evaluated with the use of the definition of the work at the disk:

$$\xi = \Delta h^0 - \frac{\Delta p^0}{\rho}. \tag{2.30}$$

As the total delta pressure Δp^0 can be reduced to static delta pressure Δp, the link between the efficiency of the stage and the previous equation is:

$$1 - \eta = \frac{\Delta p_S + \Delta p_R}{\rho \Delta h^0} \tag{2.31}$$

as detailed by N.A. Cumpsty [8].

The losses are then added to the initial work computed and a new iteration is performed. The algorithm stops when the produced thrust reaches the required thrust. The losses are computed at the middle of the blade span (at r = $(r_t + r_h)/2$).

2.2.4 Initialization of the method and loss computation

Having the required work Δh^0 and the mass flow inside the duct allows to compute the velocity triangles and thus to start the design. When the velocity triangles are obtained, the forces at the mid-span of the blades of the rotor and the stator are evaluated to find the losses. The method will be first applied to the NACA 65-210 and then to the NACA 2412.

All the initial parameters are presented in the Table 2.2.

Table 2.2 - *Parameters of the design point at cruise.*

Parameter	**Symbol**	**Value**
Thrust	T	500 N
RPM	RPM	3000 RPM
Velocity on cruise	v_∞	70 m/s
Altitude	/	2400 m
Inner radius of the fan	r_h	0.22 m
Outer radius of the fan	r_t	0.68 m
Number of blades of the rotor	n_R	5
Number of blades of the stator	n_S	8
Mass flow	$\dot{m}$	89.40 kg/s
Axial velocity	v_a	70 m/s
Jet velocity	v_j	75.6 m/s
Air density	ρ	0.97 kg/m^3
Dynamic viscosity of air	μ	1.7$\times$ 10^{-5} kg/(m/s)
Radial extend	dr	0.0047 m
Corresponding mass flow	$d\dot{m}$	0.894 kg/s

All the computed parameters at mid-span are presented for the two iterations made in Table 2.3.

Table 2.3 - *Parameters obtained using the velocity triangle at r = (r_T + r_R)/2.*

Parameter	**1st iteration**	**2nd iteration**
Δh^0	407.2 m^2/s^2	428.5 m^2/s^2
v_{u2}	2.88 m/s	3.03 m/s
β_R	-63.44 °	-63.43 °
w_r	156.56 m/s	156.49 m/s
dF_{uR}	-2.57 N	-2.71 N
c_R	0.035 m	0.037m
σ_R	0.062	0.065
dL_R	5.56 N	5.86 N
dD_R	0.09 N	0.10 N
dFa_r	-4.94 N	-5.19 N
Δp_R	374 Pa	393 Pa
α_S	1.18 °	1.24 °
v_s	70.01 m/s	70.02 m/s
c_S	0.050 m	0.053 m
σ_S	0.143	0.15
dL_S	2.57 N	2.71 N
dD_S	0.0436 N	0.0459 N
dFa_S	0.0093 N	0.0127 N
Δp_S	-0.701 Pa	-0.959 Pa
Δp_{tot}	372.9 Pa	392.056 Pa
$T_{obtained}$	492.66 N	517.97 N
$\Delta\epsilon$	21.39 m^2/s^2	22.96 m^2/s^2

As can be seen in Table 2.3, the thrust obtained with the design is not sufficient after the first iteration (only 492.66 N while the required thrust is 500 N), but is reached after the

second iteration with a value of 517 N. The input work Δh^0 in the design method will be 428.5 m^2/s^2 instead of 407 m^2/s^2. The values will be analyzed later at each radial station.

2.3 Resulting design of the rotor and the stator

Now that the losses have been evaluated, the design of the rotor and the stator along the span in performed. The obtained designs are shown in this section for both airfoils. Then the choice of the airfoil will be made. To describe the rotor and the stator, the solidity will be used. This is a dimensionless parameter that measures the fraction of the rotor disk that is covered by the blades [27]:

$$\sigma = \frac{nc}{2\pi r}. \tag{2.32}$$

2.3.1 Description of the designed blades of the rotor

The solidity and the stagger angle along the span can be observed in Fig. 2.4 and Fig. 2.5.

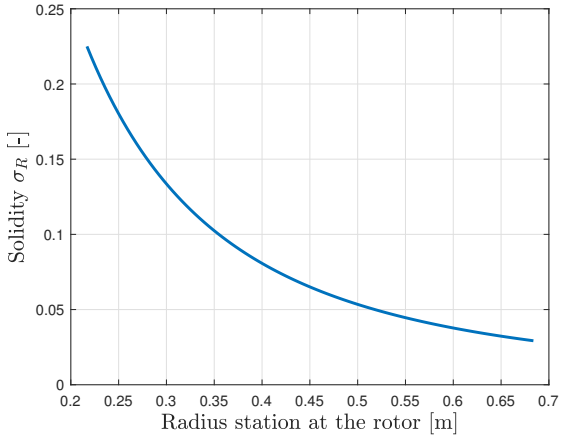

Figure 2.4 - *Solidity σ_R distribution along the span of the rotor using a NACA 65-210.*

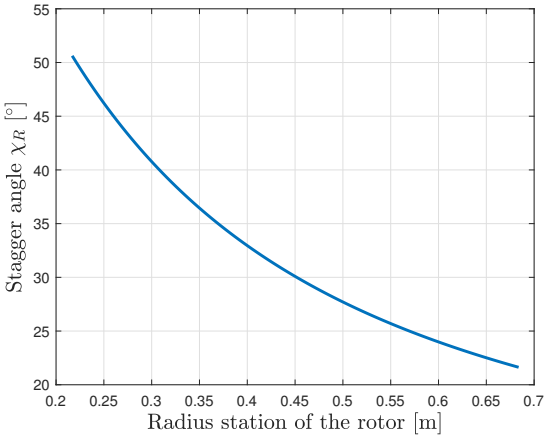

Figure 2.5 - *Stagger angle χ_R distribution along the span of the rotor using a NACA 65-210.*

As can be observed in Fig. 2.4, the solidity decreases along the span from the hub to the tip of the rotor. The maximum solidity is around 0.23 and gradually decreases to 0.03 at the tip. The stagger angle χ, as can be seen in Fig. 2.5, decreases from 51 degrees at the hub to 22 degrees at the tip. It means that the blade orientation becomes more aligned with the rotor plane towards the tip.

Having a larger solidity and a larger χ_R at the root was expected knowing that u increases linearly with the radius, it means that at low radius, u will be small and thus from the computation of χ_R in formula (2.25), it can be deduced that χ_R will be bigger so that the blade will be positioned more axially. Moreover, at higher radii, the lift is directed mostly along the axis so that it has a big contribution to the thrust, it means that less chord is required to generate the same amount of thrust.

The distribution of the chord of a blade is depicted in Fig. 2.6.

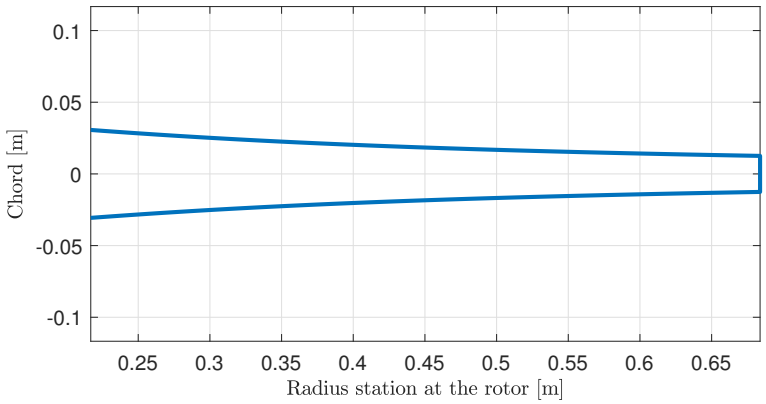

Figure 2.6 - *Chord distribution along the span of the rotor using a NACA 65-210.*

Fig. 2.6 shows the appearance of the blade if it was not twisted. The chord at the hub is 0.061 m and the chord at the tip is 0.025 m. The small value of the chord can be justified by the fact that the solidity is distributed in five blades and that the blades are not highly loaded. In this work, the structural problems will not be considered as it is mainly an aerodynamic study of the fan. Later, the rotor will be considered as an actuator disk and only the total impact of the rotor will be considered, so that only the solidity is important and not the chord of each blade separately. Anyway, if the chord is too small for the structure, three blades could be chosen, or the radius of the rotor could be reduced.

Figure 2.7 and Figure 2.8 show the distribution of the axial and tangential forces along the span of the rotor.

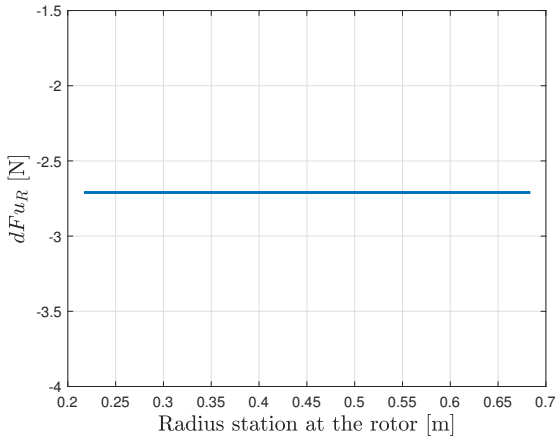

Figure 2.7 - *Distribution of the force dFu_R along the span of the rotor using a NACA 65-210.*

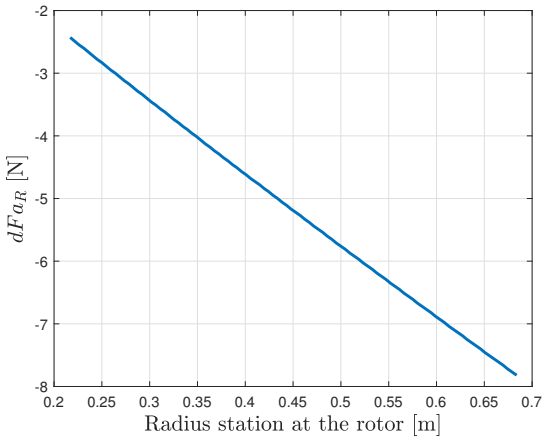

Figure 2.8 - *Distribution of the force dFa_R along the span of the rotor using a NACA 65-210.*

As can be observed in Fig. 2.7, the force dFu_R is constant along the span. It indicates that the tangential force generated by each segment dr of the blade remains uniform from the hub to the tip and that each segment contributes equally to the overall torque.

Fig. 2.8 allows so see that the force dFa_R decreases linearly from the root to the tip. As dFa_R is directly related to the thrust, it means that the generated thrust becomes larger when going to the tip. This can be explained by the fact that when going to the tip, the stagger angle χ becomes smaller so the lift is getting more aligned with the axial direction and thus contributes more to the lift than the torque.

2.3.2 Description of the designed blades of the stator

The same figures will be analyzed for the stator. The solidity and the stagger angle along the span of the stator blades can be observed in Fig. 2.9 and Fig. 2.10.

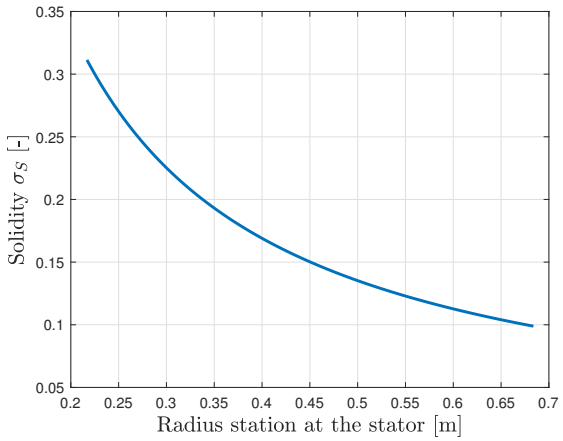

Figure 2.9 - *Solidity distribution along the span of the stator using a NACA 65-210.*

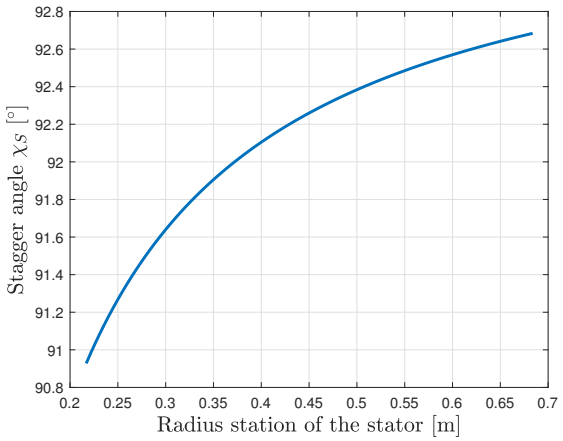

Figure 2.10 - *Stagger angle distribution along the span of the stator using a NACA 65-210.*

As can be seen in 2.9, the solidity goes from 0.31 to 0.1 along the span of the stator. As for the rotor, σ is decreasing from the hub to the tip of the blade. Figure 2.10 allows to see that the stagger angle χ_S distribution has a different behavior than the rotor. This time the χ is decreasing when going towards the tip of the blade. It was expected because the objective of the stator is to redirect the flow axially, so that the angle must be in the opposite direction to counteract the torque generated by the rotor. It can be observed that the values of χ_S are included in the range [90° - 93°] so that the chord of the blades is almost perpendicular to the tangential plane and is directed almost axially, as can be seen in Fig. 2.3.

The distribution of the chord of a blade is shown in Fig. 2.11.

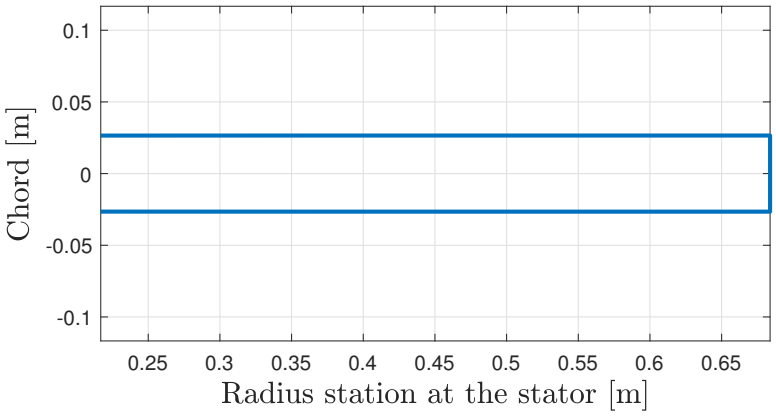

Figure 2.11 - *Chord distribution along the span of the stator using a NACA 65-210.*

It can observed from Fig. 2.11 that the chord does not vary much along the radius of the stator. This can be explained by the fact that, as the stator is not rotating, the conditions along the span are almost constant, the difference comes only from the upstream velocity vector v_u. This justifies also the small range of variation of χ_S previously mentioned.

Figure 2.12 and Figure 2.13 show the distribution of the axial and tangential forces along the span of the stator.

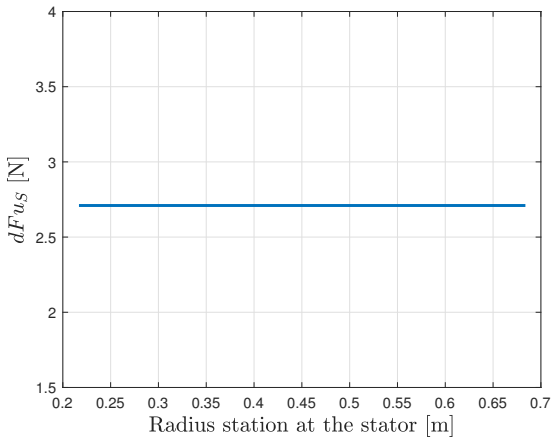

Figure 2.12 - *Distribution of the force dFu_s along the span of the stator using a NACA 65-210.*

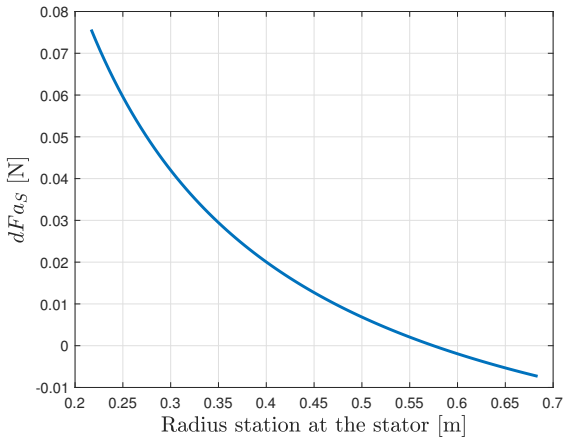

Figure 2.13 - *Distribution of the force dFa_s along the span of the stator using a NACA 65-210.*

As can be seen in Fig. 2.12, the value of the tangential force is exactly the same as the

tangential value of the rotor but with a negative sign. This was the imposed condition on the stator in order to cancel the tangential component of the velocity.

Figure 2.13 allows to see the thrust distribution along the span of the blade. It can be noticed that the values of dFa_r are positive, which means that the generated thrust is negative, and corresponds to drag. Nevertheless, the drag generated by the stator has a maximum value of 0.08 N at the root, which is really small compared to the generated thrust at the rotor, for the same blade element, which was 2.5 N. For the same reasons as before, the range of values of dFa_S is a lot smaller than the range of values of dFa_R.

In order to choose the adequate airfoil, the entire method is applied to the NACA 2412. The main results can be found hereafter. The solidity is shown in Fig. 2.14 and the stagger angle in Fig. 2.15.

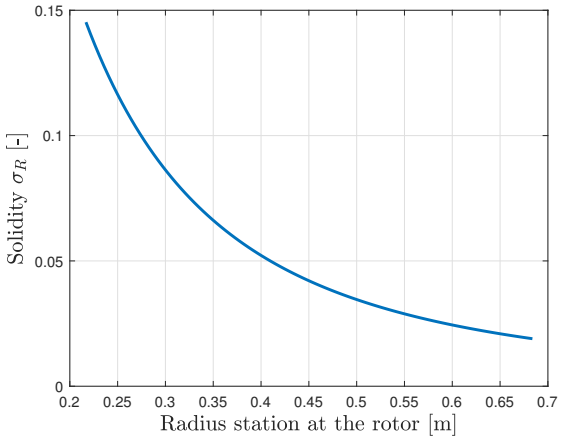

Figure 2.14 - *Solidity σ_R distribution along the span of the rotor using a NACA 2412.*

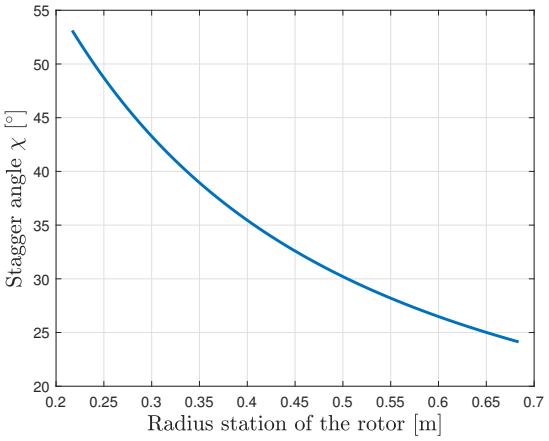

Figure 2.15 - *Stagger angle χ_R distribution along the span of the rotor using a NACA 2412.*

It can be observed that the solidity is smaller than the solidity computed for the NACA 65-210. Indeed, it goes from 0.15 to 0.02 while the range of value was of 0.23 to 0.035 for the other airfoil. This can be explain by the fact that the lift coefficient is higher for the NACA 2412 than for the NACA 65-210 (see the polars in Appendix A) so that the required chord to generate the same amount of lift has to be bigger for the NACA 65-210.
It can be seen from Fig. 2.15 that the stagger angle distribution is similar to the stagger angle distribution of the airfoil NACA 65-210.

The chord distribution can be observed in Fig. 2.16.

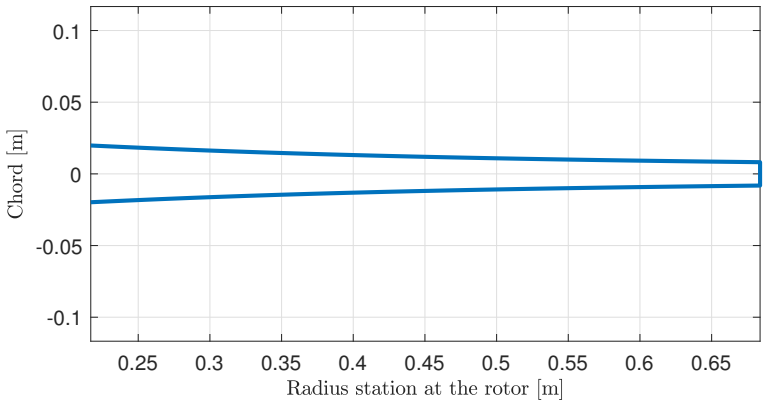

Figure 2.16 - *Chord distribution along the span of the rotor using a NACA 2412.*

As can be observed in Fig. 2.16, the chord goes from 0.04 m at the root to 0.016 m at the tip. A lower chord distribution for this airfoil was expected due to the lower solidity. Nevertheless, due to the structural problems that it could engender to have too small blade chord, this airfoil is rejected and the NACA 65-210 is chosen to be the airfoil of the rotor and the stator of the ducted fan engine.

2.4 Performance analysis

The aim of this section is to make a performance analysis of the designed rotor and stator. This section will start with a theoretical background introducing the non-dimensional parameters that will be used, followed by the performance charts derivation using a blade element method in MATLAB and its interpretation. Finally, DFDC software will be introduced and used to validate the performance charts obtained with the previously mentioned method.

To compute the generated thrust and the associated power needed, a BEM will be used, this time in the other direction as before: from the design to the performances. This is thus a classic BEM, but it has been adapted to the duct conditions. The axial velocity (v_a) is here considered to be constant inside of the duct so that the generated thrust is computed using the pressure difference and not the axial velocity difference.

2.4.1 Theoretical background

In order to do the characterization of the performances, some useful non-dimensional parameters must be introduced [17].

The performance of a propeller can be resumed in the evolution of the thrust T [N], the overall efficiency η [-], the torque C [Nm] and the absorbed power P [W] with the propeller dimensions, the properties of the air, the operational settings of the rotor and the flight velocity:

$$T, \eta, C, P = f(d; \rho, \mu, a; n, \theta; v_\infty) \tag{2.33}$$

with

- d, the diameter of the rotor [m];
- μ, the dynamic viscosity [kg/(m·s)];
- a, the speed of the sound [m/s];
- n, the rotation speed, the number of blade revolutions per second [RPS];
- θ, the collective pitch angle [°].

The collective pitch angle is a collective rotation angle of the blade around a pivot at the hub of the propeller, so that the local pitch angle $\chi(r)$ is the sum of the local stagger angle $\chi'(r)$ and the collective pitch θ[1]. The collective pitch in performance charts is often quantified by the pitch angle at three quarter span as:

$$\chi(r) = (\chi'(r) - \chi'(0.75r_t)) + \theta_{75}. \tag{2.34}$$

Thus the collective pitch angle θ that will appear in the performance graphs is defined as:

$$\theta_{75} = \theta + \chi'(0.75r_t). \tag{2.35}$$

[1] As there was no collective pitch angle in the previous section, the local stagger angle was equal to the local pitch angle and thus for the sake of simplicity denoted χ.

Knowing that these parameters all depend on three fundamental dimensions: length, mass and time, by the theorem of Vaschy-Buckingham, the relations can be reduced in five equivalent relations using only five non-dimensional parameters.

The advance ratio

The advance ratio, J is a non-dimensional parameter commonly used in propeller theory to describe the performances at various flight conditions. It describes the relation between the axial flow, represented by the flight speed (v_∞), and the tangential flow, represented by n (in [RPS]) multiplied by d, around the propeller:

$$J = \frac{v_\infty}{nd}. \tag{2.36}$$

The flow conditions can be described by two parameters, the Mach number and the Reynolds number:

$$M_u = \frac{u}{a_\infty}, \qquad \mathrm{Re}_{u,d} = \frac{\rho u d}{\mu}. \tag{2.37}$$

The performance coefficients

The performance coefficients of the propeller will be used to describe and discuss the thrust, the torque, the power and the propulsive efficiency of the rotor. The thrust coefficient is defined here related to the generated thrust as:

$$C_T = \frac{T}{d^4 \rho n^2}. \tag{2.38}$$

The torque and absorbed power are related by the relation $P = C\,\omega$, and the torque and power coefficient are defined as:

$$C_C = \frac{C}{\rho n^2 d^5} \qquad C_P = \frac{P}{\rho n^3 d^5}. \tag{2.39}$$

Finally, the propulsive efficiency is defined as:

$$\eta = \frac{C_T J}{C_P} = \frac{v_{\infty T}}{P} \tag{2.40}$$

2.4.2 Performance charts

In this thesis, the dependence on M_u and $\mathrm{Re}_{u,d}$ is neglected. The parameters that will be studied are thus C_T, C_P and η, varying with J and θ.

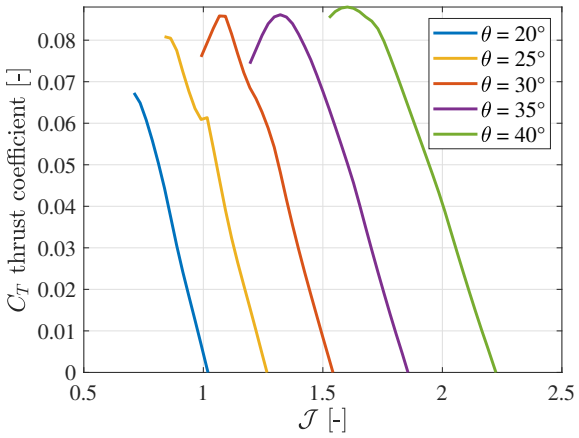

Figure 2.17 - *Evolution of the thrust coefficient C_T with the advance ratio J and the collective pitch angle θ for the NACA 65-210.*

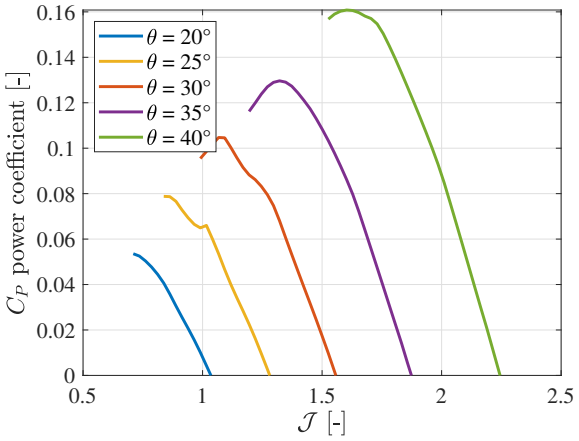

Figure 2.18 - *Evolution of the power coefficient C_P with the advance ratio J and the collective pitch angle θ for the NACA 65-210.*

In Figure 2.17, it can be seen that C_T decreases as J increases for a constant θ. This trend is anticipated because, with an increase in flight speed, the angle of attack *aoa* decreases, resulting in reduced lift, this can be deduced from the schema of the forces at the rotor, Fig. 2.2. Additionally, the advance ratio influences the flow angle relative to the blade, β_R. Therefore, as J increases, the axial velocity rises, causing the lift force to be less aligned with the axial direction, leading to reduced thrust. Concerning the variation in θ, an increase in θ causes an increase in the angle of attack, thereby generating higher thrust. For each θ, it has been observed that the C_T becomes negative when the J is high. This occurs due to the reversal of the angle of attack, resulting in the production of reverse thrust.

In Fig. 2.17, only the positive thrust coefficients are shown because the negative ones are not interesting to analyze. The range of J for each θ will only be considered for the positive thrust generation. The decrease in C_T at lower J can be explained by the shape of the polars of the airfoil NACA-65210. Indeed, at too high angle of attack part of the blade is stalling and the lift coefficient is thus decreasing, as can be observed in Fig. A.1, at an angle of attack higher than 7.75°, the lift coefficient decreases.

It can be observed in Fig. 2.18 that the power consumption for a fixed J is higher with a larger collective pitch θ. It can be explained by the fact that C_P is directly linked to the torque, and the torque depends on the flight speed and the relative angle on the blades. This coefficient also becomes negative at high J, because the negative thrust means that power is created and not absorbed (the rotor works then as a turbine and not a compressor), resulting in negative power coefficient C_P.

The global efficiency η is presented in Figure 2.19.

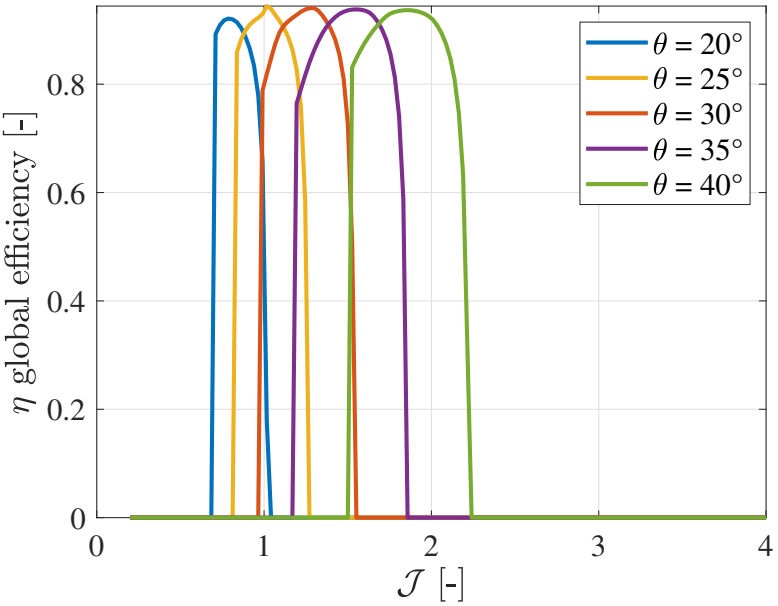

Figure 2.19 - *Global efficiency η with the advance ratio J and the collective pitch angle θ for the NACA 65-210.*

As can be seen in Fig. 2.19, the efficiency of the rotor increases as the advance ratio increases for each of the collective pitch angle. Moreover, it can be noted that η has the same comportment for each collective pitch angle θ, only shifted to higher advanced ratio as θ becomes larger so that the peak efficiency is obtained at higher advance ratio when θ is increased.
It can also be observed that the global efficiency is over 0.85 for every θ in its J-range, and abruptly goes to 0 as the thrust become suddenly negative, as previously explained.

2.4.3 DFDC software

DFDC (Ducted Fan Design Code) is a software that is used for axisymmetric analysis and design of ducted rotor. The solving method is based on a lifting-line representation of the rotor blade with an asymmetric panel representation of the duct and centerbody. DFDC is based partly on the existing propeller design code XROTOR, it combines classical propeller theory with some simple models for the effect of a duct and centerbody [23]. DFDC will be used to study and compare the performances previously computed. The designed blades of the rotor are put as an input in DFDC, as well as the aerodynamic properties of the airfoil NACA 65-210 and the dimension of the duct and the hub.

The performance charts computed using DFDC for the NACA 65-210 are presented hereafter. Figure 2.20 represents the evolution of the thrust coefficient C_T and Figure 2.21 represents the evolution of the power coefficient C_P.

The obtained C_T and C_P correspond only to the rotor part (and thus do not include the duct generated thrust) as it is the part that is willing to be study. The thrust generated by the duct will be studied later with the CFD study.

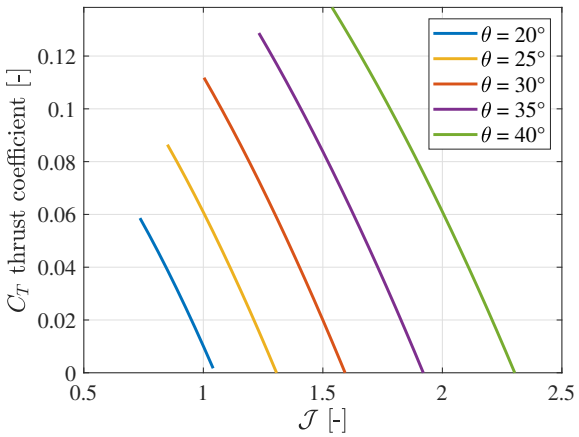

Figure 2.20 - *Evolution of the thrust coefficient C_T with the advance ratio J and the collective pitch angle θ for the NACA 65-210 using the software DFDC.*

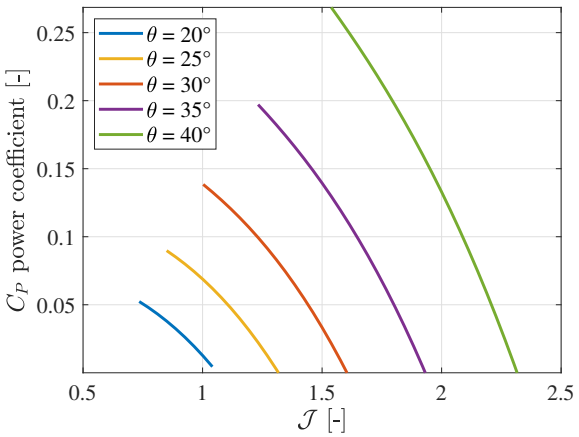

Figure 2.21 - *Evolution of the power coefficient C_P with the advance ratio J and the collective pitch angle θ for the NACA 65-210 using the software DFDC.*

As can be seen in Figure 2.20 and Fig. 2.21, the tendency of C_T and C_P is similar to the one obtained with the BEM method. However, it can be noticed that the behavior at low J is different, indeed, as the MATLAB coded BEM was using the polars, the thrust was lower at low advance ratio, in DFDC, the aerodynamics properties are not based on the polar diagram but on the curve slope $\frac{dC_L}{daoa}$ so that the stall phenomenon is not taken into account.
Finally, it can be noticed that the values of the thrust coefficient are larger than those previously observed. This can be explained by the fact that the airflow is accelerated inside of the duct so that more thrust is produced for the same corresponding advanced ratio and thus flight velocity.

The global efficiency computed with DFDC is presented in Figure 2.22.

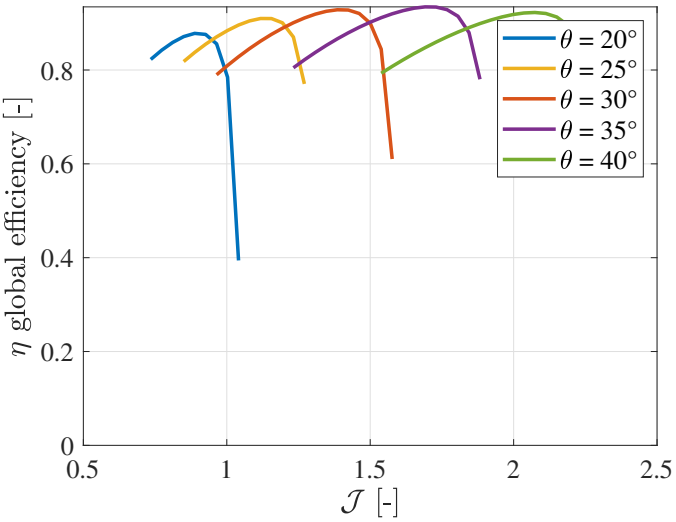

Figure 2.22 - *Global efficiency η with the advance ratio J and the collective pitch angle θ for the NACA 65-210 obtained using the software DFDC.*

The global efficiency presented in Fig. 2.22 is close to the BEM computed one. It can be noticed that the range of admitted advance ratio is wider for larger collective pitch angle than for small ones.

2.4.4 Conclusion

In this chapter, the design and the analysis of the rotor and the stator of the ducted fan system were made. The NACA 65-210 was chosen over the NACA 2412 due to the too small solidity of the NACA 2412 and the structural problems it could engender. The performance analysis allowed us to detail the generated thrust and power at different off-design points, varying the advance ratio and the collective pitch angle. It could be observed that the rotor generates less thrust at higher advance ratio for the same collective pitch angle θ, and that increasing θ leads to more thrust at same advance ratio. Those behaviors of the rotor were confirmed using DFDC software which considers the duct as well. The global efficiency was over 0.85 for every θ in its J-range. In the next chapter, the computational fluid dynamic study will be performed.

Chapter 3

CFD study of the ducted fan

The second part of this thesis consists of a Computational Fluid Dynamic (CFD) study of the ducted fan in cruise conditions. The main goal of this chapter will be to study the designed ducted fan focusing on the inlet and on the duct of the ducted fan. To do so, an actuator disk will be used to simulate the rotor in the software Ansys Fluent [4]. The objective will be to study the velocity inside the duct, the thrust generated by the duct and the performances of the ducted fan. To do this, the ULM will be studied in three dimensions with an axisymmetric condition on the upper part and in two dimensions to consider the lower part as well.

This chapter consists of a theoretical background, followed by the setup of the method, the axisymmetric case and finally the two-dimensional case, both detailed from the mesh to the results.

3.1 Theoretical background

In this section, the Reynolds number will be introduced, then the RANS model and its turbulence model will be detailed. After, the actuator disk and its pressure-jump condition will be explained from a theoretical point of view.

As explained by C. Hirsch [18], "CFD is defined as the set of methodologies that enable the computer to provide us with a numerical simulation of fluid flows." It aims to solve numerically the governing laws of motion of fluids, the Navier-Stokes equations. To perform this CFD study, Ansys Fluent will be used.

3.1.1 Reynolds number

Before talking about turbulence an important non-dimensional number which has already been introduced in the performance analysis will be redefined. The Reynolds number Re, which is widely used in aerodynamics as presented by P. Liu [22] and defined as:

$$Re = \frac{\rho u L}{\mu} \tag{3.1}$$

with

- ρ, the density of the fluid in [kg/m^3],
- u, the velocity of the fluid (here it corresponds to the flight velocity) in [m/s],

- L, a characteristic length (it corresponds here to the size of the length of the cockpit or to the chord of the duct) in [m],
- μ, the dynamic viscosity of the fluid, (it measures the fluid's resistance to shear or flow) in [kg/m/s].

The Reynolds number gives information on the transition from laminar to turbulent of the flow. It is the ratio of inertial force and viscous force of the fluid flow. A large Re means that the inertial force is greater than the viscous force and thus flow loses stability and is turbulent while a small Re means that the flow is stable, that the layers are distinct, and the flow is thus considered as laminar. The Reynolds number that represents the transition between laminar and turbulent flow is defined as 5×10^5 in the case of a flat plate at zero incidence, as presented by H. Schlichting and G. Klaus [16].

Using the values at cruise presented in the Table 2.2, and the size of the cockpit which is 3 meters or the size of the duct which is 0.8 meter, the two following Re are obtained: 1.17×10^7 and 3.1×10^6. The flow must be considered as turbulent.

3.1.2 RANS model

The Navier-Stokes equation consists in five time-dependent partial differential equations which are fully decoupled and nonlinear. To solve these equations, simplifications are introduced as semi-empirical models. The Reynolds-Averaged Navier-Stokes (RANS) model is one way to simplify the problem [22]. It is a statistical approach that resolves the mean flow while it models the fluctuations. It is thus based on average quantities, is reproducible and regular. This method is widely used for engineering analysis. It is based on the Reynolds decomposition:

$$u = U + u' \tag{3.2}$$

where u is a flow variable like velocity or pressure, U is the average quantity and u' is the fluctuation. Thus, the instantaneous flow variables are decomposed into a time-averaged component and a fluctuating component due to turbulence. RANS model solves the equation for the mean quantities, and it induces additional terms into the equations, named the Reynolds stressed, that represent the effects of turbulence of the mean flow. A turbulence model is required to model these Reynolds stresses and close the system.

3.1.3 Turbulence model

Two-equation models of turbulence have been used for most of the turbulence-model research during the past decades. As these models provide computation of k (the turbulent kinetic energy) and the turbulence length scale or an equivalent, they are complete. It means thus that they can be used to predict properties of a turbulent flow without any prior knowledge of the structure of the turbulence [35].

The first two-equation turbulence model has been proposed by Kolmogorov [16]. The two turbulence parameters he chose were the kinetic energy of turbulence, k which represents the energy contained in the turbulent eddies, and the dissipation per unit turbulence kinetic energy, ω. The interpretation of ω is described by Saffman(1970) as "a frequency characteristic of the turbulence decay process under its self-interaction". After Kolmogorov, multiple model developers made evolution on the k-ω model by changing the equation describing ω. It permitted to expand the range of its applicability and improve its accuracy [35].

A variation of this model is the SST k-ω model (Shear Stress Transport). It combines the k-ω model in the near-wall section and the k-ϵ in the free-stream region. The k-ϵ model is a commonly used model which closes the N-S system with the k and ϵ, the rate of dissipation of turbulent kinetic energy (mathematically, it is related to ω as: $\omega = \frac{\epsilon}{k}$). The SST k-ω model has the advantage of better predicting the adverse pressure gradient flows [26]. Nowadays, the SST k-ω model is an accurate, robust and reliable model that is widely used in CFD studies, it will be the turbulent model for this chapter.

3.1.4 Actuator disk and pressure-jump condition

In this study, only the rotor will be simulated. The thrust generated by the stator is thus neglected, which is not a bad approximation knowing that the stator generated thrust is really small. Furthermore, the objective of the stator is mainly to provide support to the duct and to redirect the flux after the rotor, and in this CFD study, the structure will not be analyzed nor the part of the flux located after the duct.

To simulate the rotor, an actuator disk will be used. It is a theory used to simulate the effects of a rotor, making abstraction of the actual geometry of the blades and the detailed flow near them. This theory will be explained based on the course note from K. Hillewaert (2023) [17] adapted to ducted propeller.

An example of the pressure-jump is shown in Figure 3.1.

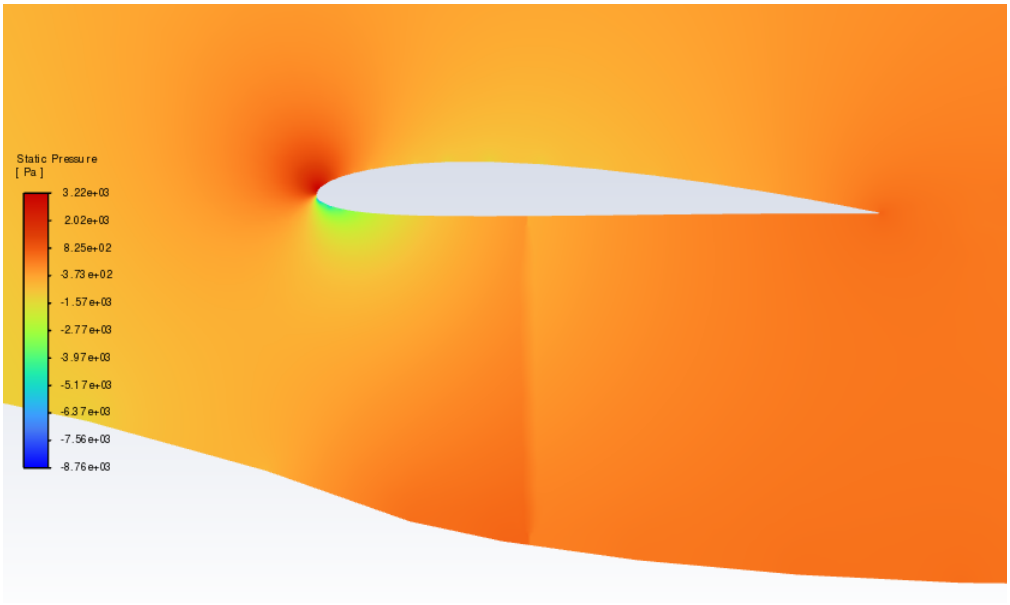

Figure 3.1 - *Illustration of the pressure-jump at the actuator disk.*

The actuator disk theory is a mathematical model that uses the conservation laws of mass, linear momentum and energy to determine the ideal performance of an energy-adding or an energy-extracting device, such as a propeller or a turbine, in a flow stream that is steady, inviscid, one-dimensional and incompressible. It makes the hypothesis that the flow is homogeneous across any normal section of the flow.

The hypotheses of the theory are the listed hereafter.

- The flow velocity and pressure are assumed as constant in any section normal to the flow in the stream tube of the rotor.

- The propeller will induce a sudden change of the flow conditions. The change in total condition can be described as:

$$\frac{\Delta p^0}{\rho} = \frac{p_+ - p_-}{\rho} + \frac{v_{a+}^2 - v_{a-}^2}{2} + \frac{v_{u+}^2 - v_{u-}^2}{2} \tag{3.3}$$

  with

  - $\Delta\, p^0$ the change in total pressure;
  - p_- and p_+ the static pressure before and after the disk;
  - v_{a-} and v_{a+} the axial velocities before and after the disk;
  - v_{u-} and v_{u+} the tangential velocities before and after the disk.

  As the change in tangential velocity can be considered negligible (due to the high rotation speed) and the change in axial velocity is zero due to the conservation of mass, the effects of the propeller are reduced to a jump in static pressure only.

- The far up- and downstream pressure are equal to the ambient pressure.

The flow conditions along the duct are resumed in Figure 3.2.

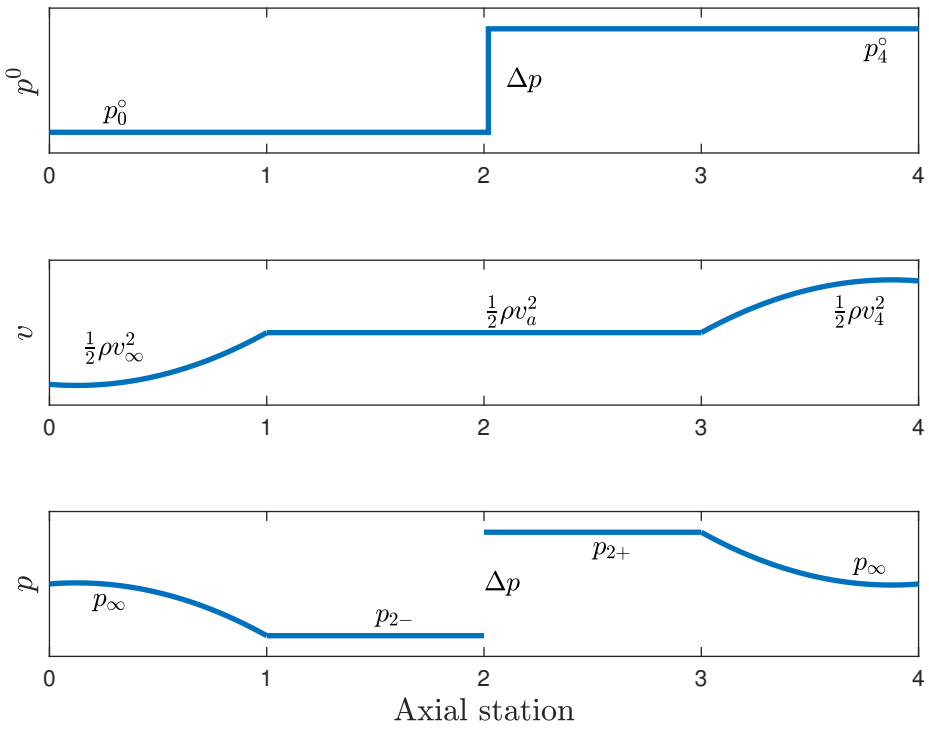

Figure 3.2 - *Flow conditions along the axial direction.*

In Figure 3.2, the axial stations are the following:

- 0: farfield upstream conditions;
- 1: entry of the duct;

- 2: actuator disk position;
- 3: exit of the duct;
- 4: farfield downstream conditions.

The upper graph represents the total pressure, the middle graph represents the dynamic pressure, and the lower graph represents the static pressure. As can be seen in the figure, the effect of the actuator disk (AD) is a sudden jump in total pressure. The two lower graphs decompose the total pressure in the dynamic pressure, which corresponds to the kinetic energy of the fluid, and the static pressure, which corresponds to the pressure of the fluid at rest. In the middle graph of Fig. 3.2, it can be seen that the kinetic energy remains constant inside of the duct, it is due to the fact that the axial velocity remains constant, because of the conservation of mass inside of the duct. The last graph allows to see that, due to the hypotheses, the total pressure-jump can be reduced to the static pressure-jump at the AD station.

To simulate the rotor, the pressure-jump must be defined. Neglecting Reynolds effect, the pressure difference only depends on two variables such that:

$$\frac{\Delta p^0}{\rho} = f(J, \theta) \tag{3.4}$$

with J the advance ratio and θ the collective pitch angle. Neglecting the Reynolds effects allows to study the rotational speed of the rotor and the free stream velocity together and not separately.

The pressure-jump is computed using the thrust T obtained at specified J and θ from the BEM analysis as:

$$\frac{\Delta p^0}{\rho} = \frac{T(J, \theta)}{A\rho}. \tag{3.5}$$

The curves obtained in the performance analysis and shown in Fig. 2.17, are approximated using a polynomial interpolation. Those curves will be entered as fan conditions in Ansys Fluent to simulate the rotor.

3.2 Setup and practical application

The objective of this CFD study is to make an axisymmetric simulation of the rotor using the upper part of the ULM and a two-dimensional simulation of the model. The goal of this section will be to make the setup of those two simulations. The mesh will be detailed, from the quality parameters to the boundary layer using the y+ condition.

To obtain the two-dimensional domain of the Mindus Belvedere ULM, the CAD is cut along its median plane as shown in Figure 3.3.

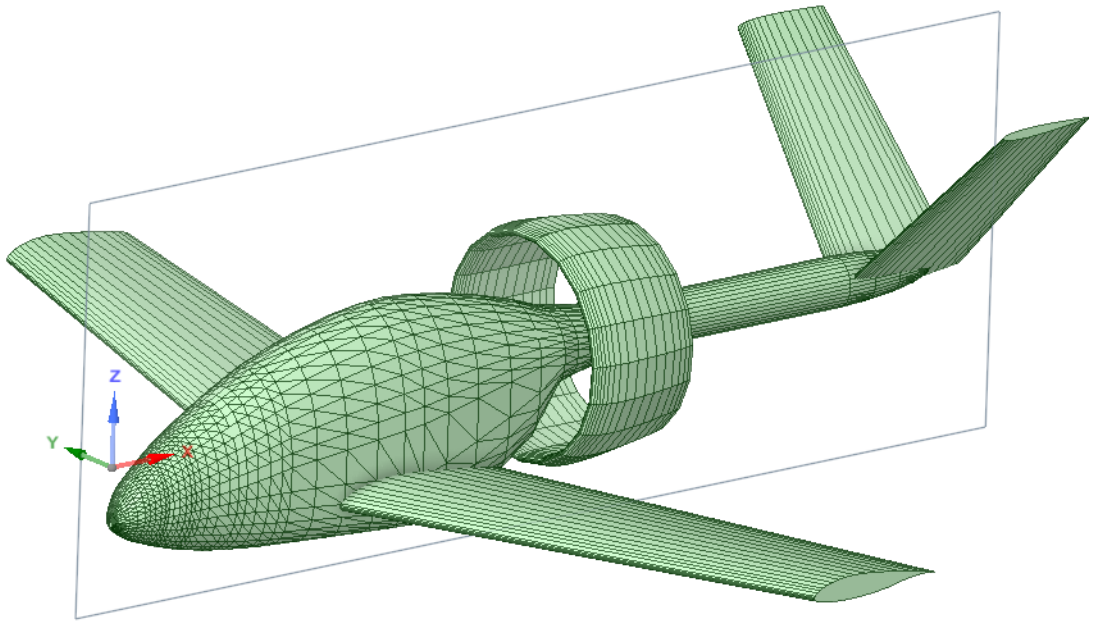

Figure 3.3 - *CAD of the Mindus Belvedere ULM and cutting plan.*

3.2.1 Boundary conditions

The imposed boundary conditions on the fluid domain in Ansys Fluent can be found in Table 3.1.

Table 3.1 - *Boundary conditions imposed in Ansys Fluent.*

Location	Imposed condition	Details
At the duct	Wall condition	No slip condition
At the cockpit	Wall condition	No slip condition
At the inlet	Axial velocity	Flight velocity v_∞
At the outlet	Static pressure condition	Atmospheric pressure
At the fan	Fan condition	Pressure-jump
At the farfield	Axial velocity	Flight velocity v_∞

At the cockpit and the duct wall, a wall condition is imposed as a no slip condition. It means that the fluid velocity at the wall is zero relative to the wall. At the inlet, the flight velocity is imposed axially, as it represents the conditions in cruise, the same condition is imposed at the farfield. This condition will vary as the advance ratio J varies. At the outlet, the pressure is set to the atmospheric pressure at 2400 m which is the cruise altitude. At

the fan, a fan boundary condition is imposed as a pressure-jump across its boundary. The pressure-jump is specified as polynomial, varying with the axial velocity at the fan. For each θ-curve, a different polynomial relation between the pressure-jump and the velocity is set. The range of velocity is limited by the range of J computed previously for each θ. The pressure-jump is calculated from the average axial velocity conditions at the disk; thus it does not vary along the radius of the rotor.

3.2.2 Mesh

To ensure a good mesh, four quality parameters will be used. The description of those parameters is made using Ansys Fluent Users Guide [5] and the course notes from V. Terrapon (2023) [31].

Orthogonal quality

The orthogonal quality measures how perpendicular the faces of the mesh cells are to each other and the lines of the grid. It is computed as the dot product between the vectors that connects the center of two neighboring cells and the cell face normal. If the orthogonality is close to 1, it implies that the cells are well-aligned and thus that the results will be more accurate in the gradient calculations. The minimum orthogonal quality gives information on the worst-case of cell alignment. The orthogonality is ideally greater than 0.7 and will be rejected if lower than 0.1 because it may cause instability.

Maximum aspect ratio

The maximum aspect ratio is the ratio between the longest and the shortest edge of a mesh element. Having stretched cells and thus a high aspect ratio can lead to instability and numerical diffusion, which is the unintended spreading of a physical quantity in the computational domain. Having large aspect ratio in the boundary layer region is acceptable, because the cells are aligned with the flow direction and thus the gradient along the large edge is rather small. An acceptable aspect ratio is 10 for the unstructured mesh and, as there is a boundary layer, to 100 is considered as acceptable.

Skewness

The skewness gives information on the deviation of an element from being perfectly orthogonal for the quadrilateral elements or equilateral for the triangle elements. A low skewness is better, and the acceptable range is between 0.25 and 0.5.

Mesh element type

The type of element in the mesh has its importance in the accuracy of the results. In general, the quadrilateral elements are preferred because they align with the flow and provide a higher accuracy. Triangular elements are common in unstructured mesh having complex geometries. In this work, the elements will be chosen to be mostly quadrilateral and the gaps due to the geometry will be filled with triangular elements.

3.2.3 Y+

The term y^+ is a dimensionless value used in fluid dynamics to quantify how well a mesh captures the viscous sub-layer near a wall in a turbulent flow. This sub-layer is characterized by a nonlinear velocity profile, which is important to accurately simulate wall-bounded

flows.

Physically, y^+ represents the non-dimensional distance from the wall and is defined as:

$$y^+ = \frac{yu_\tau}{\nu} \tag{3.6}$$

where:

- y is the physical distance from the wall in [m],
- u_τ is the friction velocity [m/s],
- ν is the kinematic viscosity of the fluid [m^2/s].

The friction velocity u_τ is given by:

$$u_\tau = \sqrt{\frac{\tau_w}{\rho}} \tag{3.7}$$

where:

- τ_w is the wall shear stress in [N/m^2] or [Pa];
- ρ is the fluid density in [g/m^3].

In computational fluid dynamics, it is important to determine the appropriate size of the cells near the wall to accurately capture the velocity gradients within the viscous sublayer. A common guideline is to have the first cell height in the mesh correspond to a y^+ value of around 1. This ensures that the mesh is fine enough to resolve the steep velocity gradients near the wall without excessive computational cost.

To estimate y^+ before running a simulation, preliminary calculations based on expected flow conditions are used. After the simulation, y^+ will be analyzed as an output to verify that the mesh resolution near the wall was appropriate. If the calculated y^+ values do not fall within the desired range, the mesh may need refinement.

3.3 Axisymmetric simulation

In this section, the domain and the boundary conditions will be detailed, the mesh will be presented and finally, the results of the simulation will be studied.

3.3.1 Domain and Boundary conditions

The domain of the axisymmetric study is obtained using the cutting plan on the CAD as shown in Figure 3.3 and taking the part that takes place above the center of the disk. The plan must be cut exactly in the center of the duct to be able to perform the axisymmetry. The obtained domain is shown in Figure 3.4.

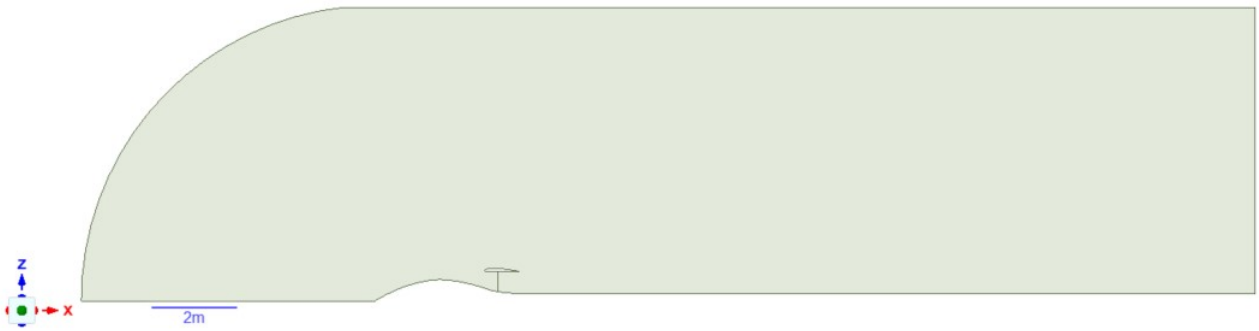

Figure 3.4 - *Fluid domain of the axisymmetric simulation of the ULM.*

As can be seen in Fig. 3.4, the part that takes place after the duct has been slightly modified. Indeed, the fuselage of the ULM is extended to the outlet (at the right of the picture). This was made to study only the effects before and at the duct. In this study, the effects on the V-tail and after the duct in general will not be studied. A line is added to the geometry at 0.3 meter of the entrance of the duct, it will be used as the actuator disk.

Due to the axisymmetry, a boundary condition is added to the ones presented in Table 3.1, an axis condition is put as symmetry axis at the lower left part of the domain that can be seen in Fig. 3.4. This will ensure that the center of the axisymmetry is at the center of the rotor.

Figure 3.5 provides a better view of the cockpit and the position of the actuator disk.

Figure 3.5 - *Zoom on the fluid domain of the axisymmetric simulation of the ULM.*

3.3.2 Mesh of the axisymmetric simulation

The total mesh of the fluid domain of the axisymmetric simulation is shown in Fig. 3.6.

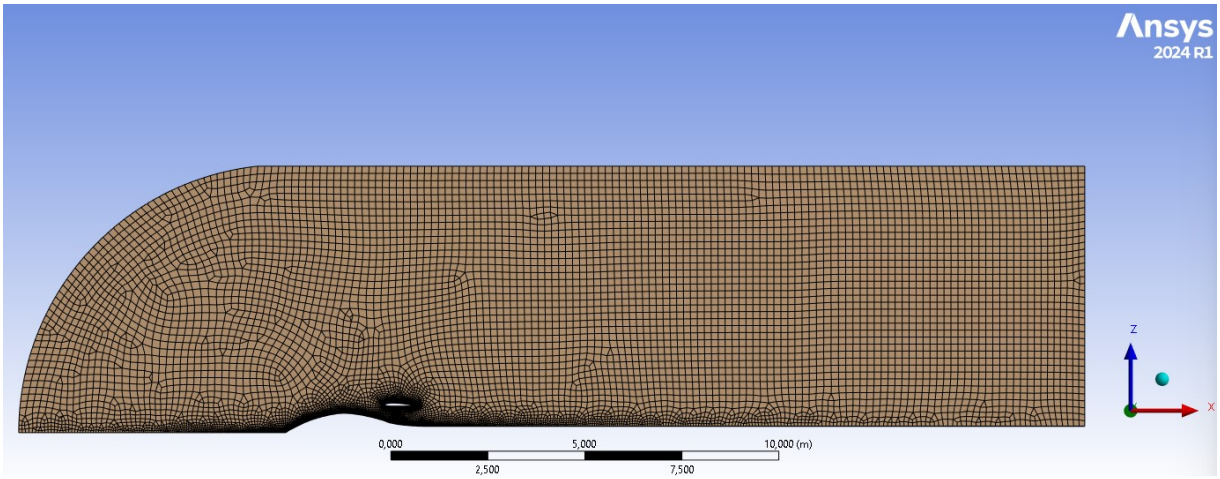

Figure 3.6 - *Mesh of the fluid domain of the axisymmetric simulation.*

As previously introduced, the y+ condition must be considered. A first estimation of the required size of the mesh is made using the flat-plate boundary layer theory [33]. For the duct, the input values are the U_∞ which is the freestream velocity: 70 m/s. The freestream density and dynamic viscosity are those of the air at 2400 m (the cruise altitude). The reference length is 0.8 m: the chord length of the duct. The desired y+ is fixed to 1 and the resulting maximum for the first cell height thickness is 0.0065 mm. The mesh will thus be refined in the near-wall region. For the y+ of the BL situated in the cockpit, the reference length is 3 m, and the obtained size of the mesh required is 0.0072 mm.

To apply the y+ precisely, the function "first layer thickness" of the meshing condition "inflation" is chosen in Ansys Fluent. The first layer is thus chosen to 0.006 mm and 0.007 mm. As it is better to have a smooth transition from one element to the other, (because some computation will be made based on the derivative along y) the size of the elements outside of the boundary layer zone are adjusted.

A zoom on the mesh near the wall of the duct is shown in Figure 3.7.

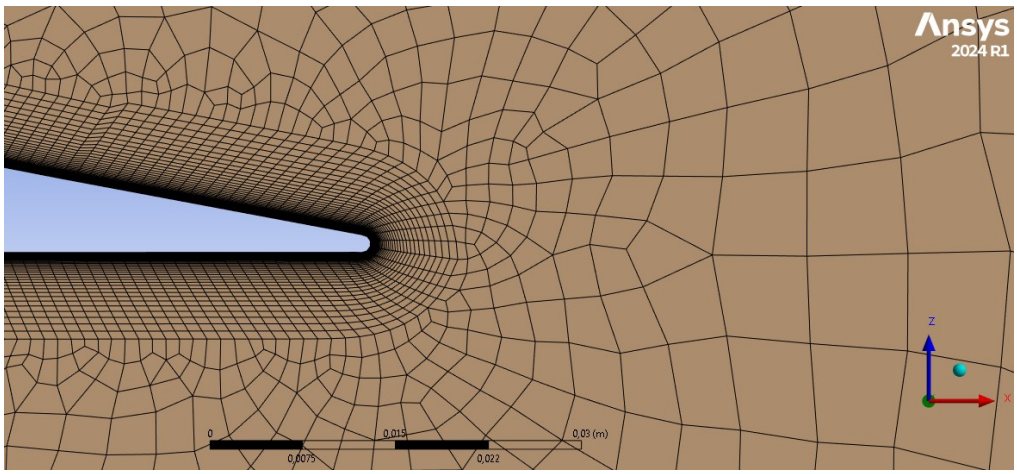

Figure 3.7 - *Zoom on the boundary layer of the duct of the mesh of the fluid domain of the axisymmetric simulation.*

It can be observed in Figure 3.7 that the elements are mostly quadrilateral and that the mesh is progressively refined to smoothly end in a really thin height of element at the boundary layer. Figure 3.8 shows a zoom at the actuator disk zone of the mesh.

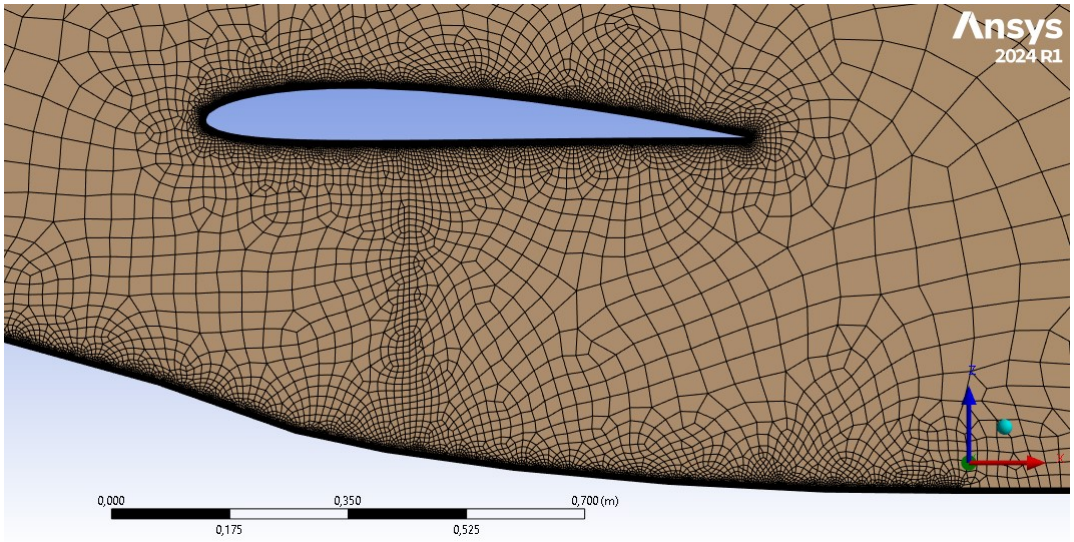

Figure 3.8 - *Zoom on the boundary layer of the duct of the mesh of the fluid domain of the axisymmetric simulation.*

As can be observed in Fig. 3.8, the mesh is refined in the zone of the actuator disk and in general near the walls.

The characteristics of the mesh are analyzed following the criterion explained in the previous section. The element type are detailed in Table 3.2. It can be observed that only 0.14 % of the elements are triangular which fulfill the element criterion.

Table 3.2 - *Characteristics of the elements of the mesh of the axisymmetric simulation.*

Type of elements	quantity
TriShell3	310
QuadShell4	220158
Total	220468

The quality mesh is given by Ansys Fluent in the form of distribution for the mesh elements, it can be seen in the following charts, Figure 3.9 for the distribution of aspect ratio, Figure 3.10 for the orthogonal quality and Figure 3.11 for the skewness.

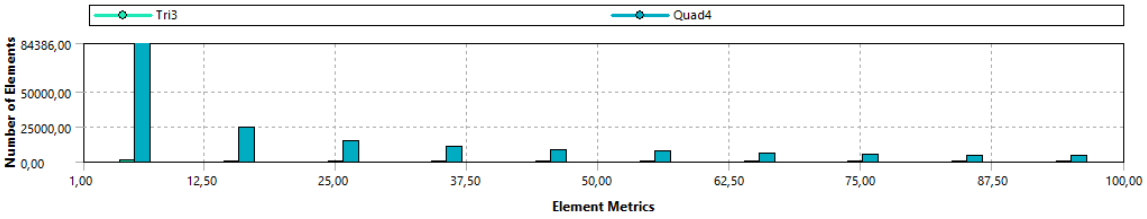

Figure 3.9 - *Distribution of the aspect ratio for triangular (Tri3) and quadrilateral (Quad4) mesh elements.*

Using the meshing tool in Ansys fluent, it could be observed that the maximum aspect ratio of the mesh occurs as the boundary layer of the duct and of the cockpit which was expected due to the y+ condition imposed. It can also be seen that most of the aspect ratio is below 10, and that the elements having an aspect ratio above 10 were included in the boundary layer.

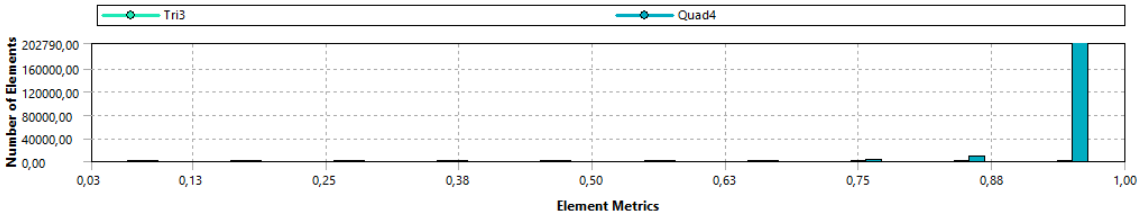

Figure 3.10 - *Distribution of the orthogonal quality for triangular (Tri3) and quadrilateral (Quad4) mesh elements.*

From Figure 3.10, it can be seen that most of the orthogonal parameters have a value above 0.88 and all of them have a value superior to 0.75 which validate the orthogonality criterion.

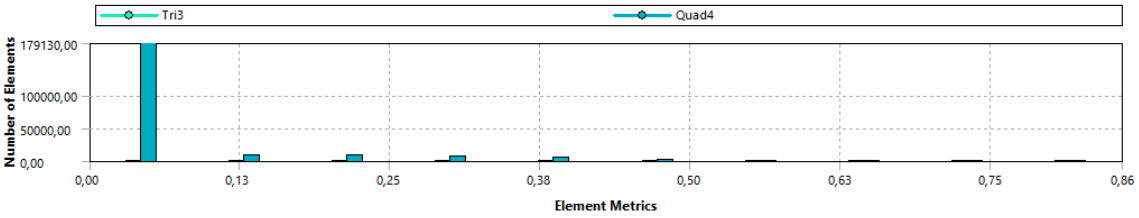

Figure 3.11 - *Distribution of the skewness for triangular (Tri3) and quadrilateral (Quad4) mesh elements.*

It can be observed in Figure 3.11 that the skew parameter is mostly lower than 0.13 and that all the elements have a skewness below 0.5.

This mesh is thus validated as it respects the four imposed quality criteria.

3.3.3 Results of the axisymmetric simulation

The results obtained with the axisymmetric simulation will be divided in three sections, first the results in terms of velocity and pressure in cruise conditions, then the thrust and drag forces will be analyzed also in cruise conditions and finally the performance charts will be reproduced with the updated axial velocity and the thrust generated by the duct will be analyzed.

Velocity and pressure analysis

The velocities will be analyzed in their axial component, as shown in Figure 3.12 and in their radial component, as shown in Figure 3.13. The pressure is separated in total pressure distribution in Figure 3.14 and static pressure distribution in Figure 3.15.

Figure 3.12 - *Axial velocity (along x) in axisymmetric and cruise conditions.*

Figure 3.12 shows the axial velocity distribution which represents the velocity in the direction of the flight velocity imposed at the inlet. It can be observed that this velocity is mainly constant before the cockpit, then the flow is decelerated to almost 0 m/s when encountering the left limit of the cockpit which corresponds to a stagnation point. Then it is accelerated when arriving at the top of the cockpit with a velocity magnitude of 85 m/s and finally decelerated again (without reaching negative values) when at the hollow of the cockpit. Moreover, it can be observed that the velocity is higher inside of the duct than outside, the flow is thus accelerated when entering the duct. A second stagnation point is observed at the leading edge of the duct.

Figure 3.13 - *Radial velocity (along y) in axisymmetric and cruise conditions.*

Figure 3.13 allows to study the radial velocity, which is the velocity perpendicular to the flight velocity. It is observed that the radial velocity before the cockpit is 0 then is accelerated to 28 m/s along the cockpit due to its geometry and afterwards becomes negative to -20 m/s to go down along the cockpit. This figure allows to confirm the two stagnation points as it can be observed that the radial velocity is also 0 at those two points.

Figure 3.14 - *Total pressure distribution in axisymmetric and cruise conditions.*

The total pressure distribution can be observed in Figure 3.14. The total pressure is mainly constant, and the pressure-jump is observed at the AD. The total pressure tends to highly negative values at the leading edge of the duct.

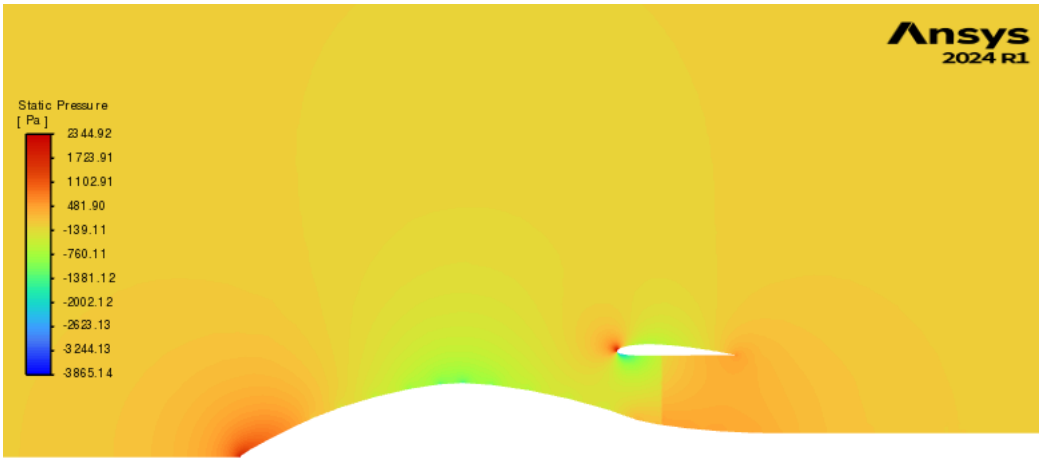

Figure 3.15 - *Static pressure distribution in axisymmetric and cruise conditions.*

The static pressure distribution can be observed in Figure 3.15. The value is 0 almost everywhere as it is the change in pressure that matters, the value of the pressure can thus be set up to an arbitrary constant. In the software, the operating conditions are put at 2400 m, thus with an atmospheric pressure of 75625.68 Pa.
The pressure-jump can be observed. The expected behavior, presented in Figure 3.2 can be seen. Indeed, the static pressure decreases and is negative before the AD, then suddenly becomes positive stays a bit constant in the duct and then decreases to 0 after the duct.
It can also be observed that the two identified stagnation points correspond to the points with the highest static pressure value. Which is expected as the dynamic pressure is converted to the static pressure.

Thrust and drag computation

In this section, the thrust and drag component will be detailed. First with the actuator disk thrust, then the duct generated thrust and finally the drag generated by the cockpit.

The total thrust generated by the ULM will be decomposed in two contributions. The thrust generated by the actuator disk and the trust generated by the duct.

To compute the thrust generated by the disk, the mean axial velocity at the disk must be extracted from the Ansys Fluent simulation because contrary with the hypotheses made to perform the design, the axial velocity is not equal to the flight velocity, so that the pressure-jump depends on the conditions at the AD and not the imposed inlet velocity. With the use of the axial velocity at the disk, the pressure-jump is extracted from the performance curves computed with the BEM and put in the CFD simulation. To reproduce the entire thrust coefficient curve for each collective pitch angle, four to five points will be used varying the flight velocity in the inlet condition for each curve. In the operating point, the thrust at the actuator disk is, $T_{AD} = 413.9$ N.

The thrust generated by the duct is computed using the drag tool in Ansys Fluent. In the case that the obtained value is negative, it means that it corresponds to a thrust generated by the duct, otherwise it is a drag force. In the case of the operating point, the obtained thrust, T_{duct} is 19.6 N.

The drag generated by the surface of the cockpit is computed using the drag tool in Ansys. At the design point, this value is 197.2 N. All the forces previously computed and some more output parameters are summarized in Table 3.3.

Table 3.3 - *Thrust and drag computed from the axisymmetric simulation at the design point: cruise condition: 2400m and $v_\infty = 70$ m/s.*

Force	T_{AD}	T_{duct}	T_{tot}	$D_{cockpit}$
Value	413.9 N	19.6 N	433.52 N	197.2 N

The total thrust, defined as the sum of the two components previously detailed, is close to the real total thrust of the ULM. The only difference comes from the inlet of the rotor which is here considered as axisymmetric even though it is not the case in the real geometry. It can be observed from Table 3.3 that the duct is giving a contribution of 4.5 % of the total thrust, which is a good result knowing that, as presented in the introduction, having a duct is mostly advantageous at low airspeed, and in general for the static thrust.

For the drag, only a small contribution to the total drag can here be computed, first because the cockpit drag is underestimated (as the upper part is less likely to produce drag than the lower part, due to its shape) and then because the drag generated by the wings and the tail are not considered as they are not present in the simulation.

Table 3.4 - *Mass flow and axial velocity from the axisymmetric simulation at the design point: cruise condition: 2400m and $v_\infty = 70$ m/s, with and without actuator disk.*

AD	$\dot{m}_{AD}$	$v_{a_{duct}}$
with	91.4 kg/s	71.6 m/s
without	84.9 kg/s	66.5 m/s

Table 3.4, allows to see the mass flow rate and the axial velocity with and without the

actuator disk. It allows to see the effect of the engine on the mass flow inside of the duct, and thus the axial velocity inside of it (located at the AD). It can be observed that this axial velocity, $v_{a_{duct}}$ is larger than the flight velocity, v_∞. It is due to the airfoil shaped duct and the fact that the mass flow is drawn into the duct by the pressure difference of the fan.

Performance analysis of the axisymmetric simulation

To study the thrust properly, the same non-dimensional parameter will be studied to analyze the thrust: the thrust coefficient C_T, varying with the advanced ratio J. First, the performance graph from the design chapter will be compared to the real performances, considering the real axial velocity. Then the thrust generated by the duct will be analyzed.

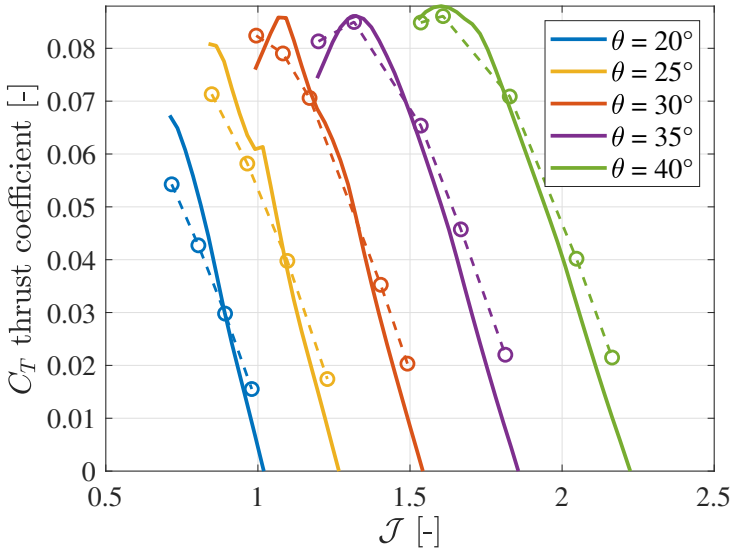

Figure 3.16 - *Thrust coefficient C_T at different collective pitch angles (θ) from Fig. 2.17 in solid lines, and the corresponding values in dashed lines computed using Ansys Fluent.*

In the Figure 3.16, the solid lines represent the C_T of the previously designed fan from Fig. 2.17 and the dashed lines with circle represent the points computed using Ansys Fluent. Each color represents a different collective pitch angle θ. To better do the comparison, only the actuator disk thrust is taken into account for the Ansys C_T curves.

It can be observed from Figure 3.16 that the points computed with Ansys have a lower thrust coefficient C_T at low advance ratio J while they have a higher C_T at higher J, compared to the initial curves. To understand this behavior, the velocity inside of the duct must be studied.

The velocity difference between outside and inside of the duct is shown in Figure 3.17.

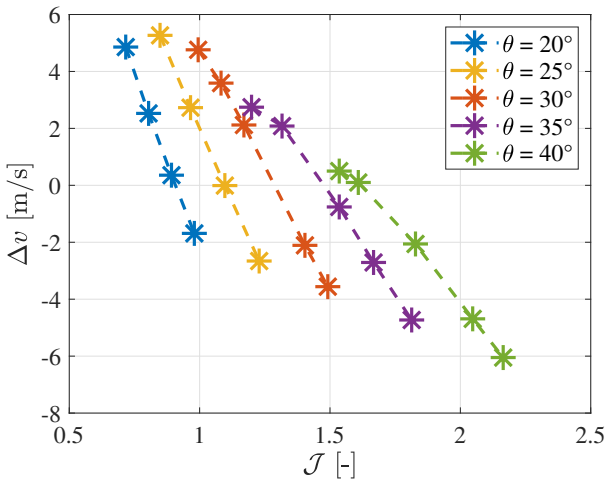

Figure 3.17 - *Difference of the velocity inside of the duct and the flight velocity:* $\Delta v = v_\infty$ - $v_{a_{duct}}$ *at various* θ *computed with Ansys Fluent.*

The velocity difference observed in Fig. 3.17 is defined as the difference between the flight velocity and the axial velocity at the disk (thus inside of the duct). For the same J in the first half of the J-range, the air is accelerated inside of the duct while for the second half of this range, the air is decelerated inside of the duct. It thus explains that for the lower part of the range, the performance curve shown in 3.16 are shifted to the left while the second part is shifted to the right, knowing that for the BEM computed performance curves, the axial velocity is assumed to be the flight velocity. Finally, it can be observed that the stall phenomenon that occurs at the low J part of the curves, is less likely to happen because of acceleration of the axial velocity.

Figure 3.18 shows the total thrust coefficient at the various collective pitch angles θ computed with Ansys Fluent.

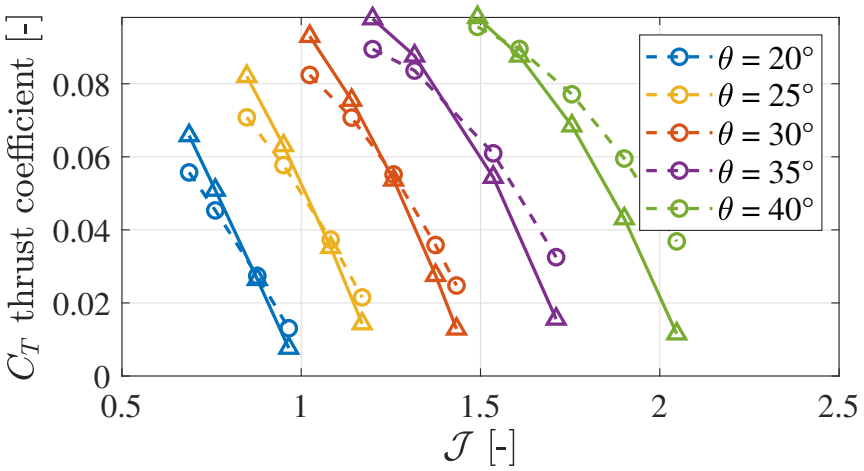

Figure 3.18 - *Thrust coefficient* C_T *at various collective pitch angles* (θ)*, computed using Ansys Fluent, with the duct in full lines and without the duct in dashed lines.*

In the Figure 3.18, the solid lines represent the total C_T, computed with the total

generated thrust (thus by the duct and by the actuator disk) and the dashed lines represent, as in Fig. 3.16, the C_T computed only with the AD-generated thrust. Each computed point is depicted with a circle or a triangle.

As can be seen on the graph, when the advanced ratio J is in his higher range, the C_T-curve including the duct is below the curve computed without the duct while it is the opposite at lower J. This can be explained by the fact that the thrust generated by the duct becomes negative at higher flight velocity. This phenomenon can be observed in Fig. 3.19. It confirms the hypothesis that the duct is mainly advantageous at low fight velocity.

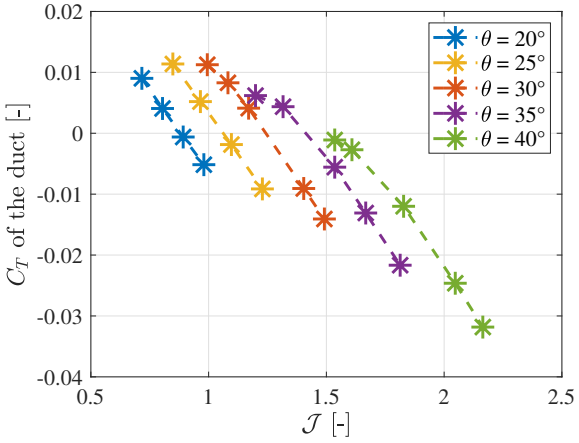

Figure 3.19 - *Thrust coefficient C_T of the duct at various θ computed with Ansys Fluent.*

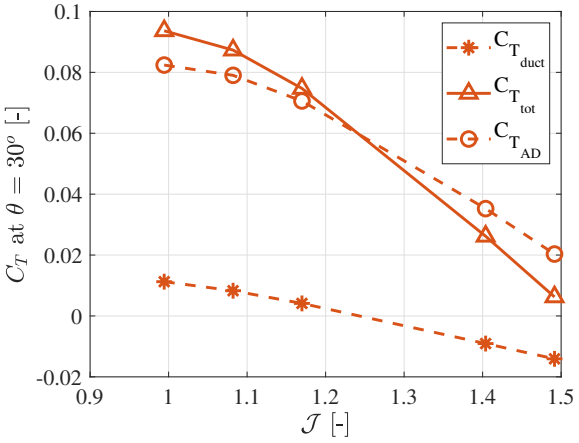

Figure 3.20 - *Thrust coefficient C_T at $\theta = 30°$ computed with Ansys Fluent.*

Fig. 3.19 and Fig. 3.20 allow to study more clearly the effects of the duct. From Figure 3.19 it can be seen that the thrust generated by the duct becomes negative at the half of the J range for the low θ and the range of positive duct generated thrust in the J range becomes smaller when θ is higher. For example, it can be observed that the duct almost never generates thrust in the case of a $\theta = 40°$. Having a duct is thus not advantageous in that range of parameters.

Fig. 3.20 shows the total thrust coefficient $C_{T_{tot}}$ for a $\theta = 30°$ and its two contributions: from the duct with $C_{T_{duct}}$ and from the actuator disk with $C_{T_{AD}}$. For a J of 1, the duct has a positive contribution of 11 % of the $C_{T_{tot}}$ while for $J = 1.43$, the duct has a negative contribution that is close to the positive contribution of the AD to the thrust so that $C_{T_{tot}}$ get close to 0, with a value of 0.00049.

3.4 Two-dimensional model simulation

To study in more details the integration of the duct with the cockpit, a new two-dimensional model will now be implemented. This time the down part will be considered as well as the upper part of the cockpit. The simulation will be done at cruise conditions and with the pressure-jump of the fan at designed conditions. The objective of this section is to compare the two different inlets of the rotor. The mesh will first be studied and then the results will be analyzed, for the velocity and pressure and then for the inside duct velocity.

The domain of this simulation is obtained using the same cutting plan on the CAD, shown in Figure 3.3. The tail and the wing are thus not part of the simulation. The boundary conditions of the simulation were presented in Table 3.1.

3.4.1 Mesh of the two-dimensional model

The mesh of the fluid domain of the two-dimensional simulation is shown in Figure 3.21.

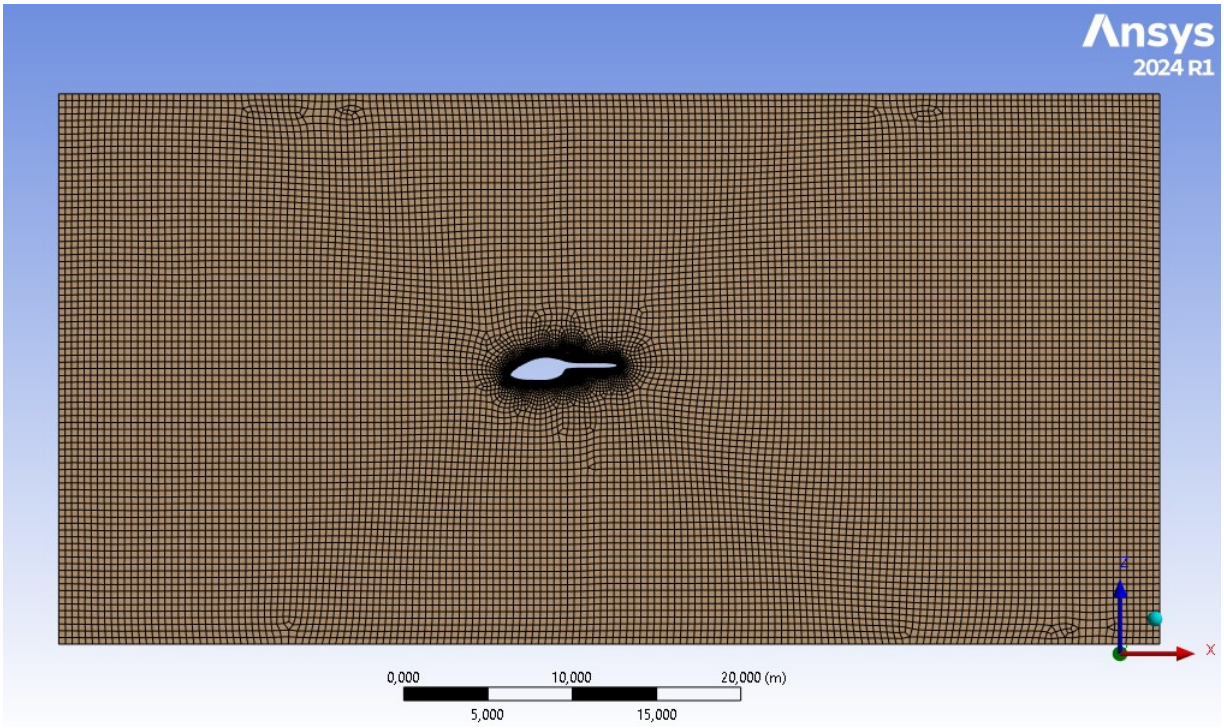

Figure 3.21 - *Mesh of the fluid domain in the two-dimensional model simulation.*

The y+ has been considered the same way as in the axisymmetric simulation, with thus a "first layer thickness" condition in the mesh tool of Ansys Fluent. A zoom on the mesh near the airplane is shown in Figure 3.22.

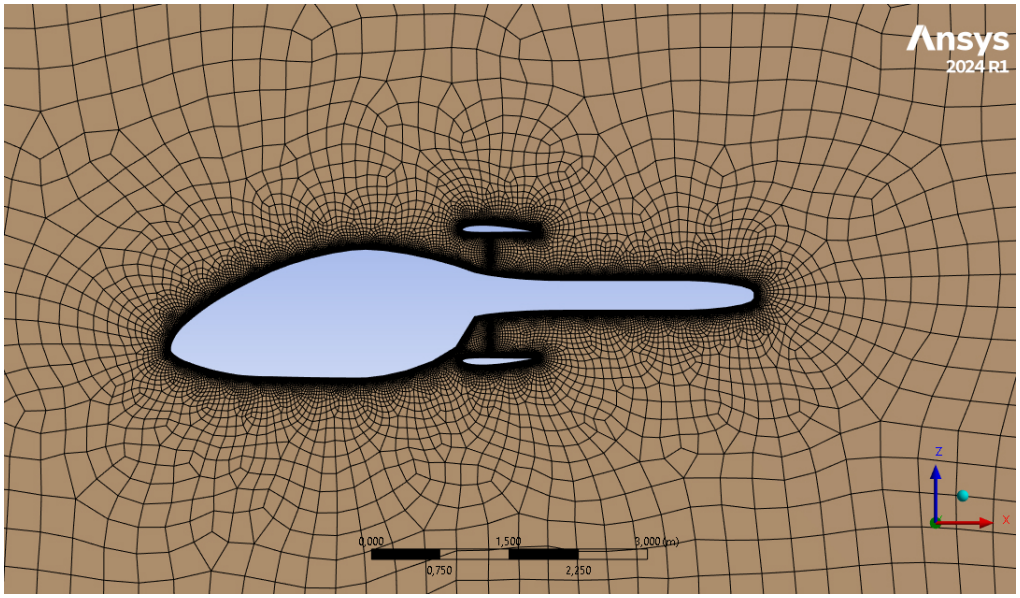

Figure 3.22 - *Zoom on the mesh around the ULM of the fluid domain in the two-dimensional model simulation.*

It can be observed that the mesh becomes finer closer to the walls. It can also be observed that the lower part of the cockpit is very different from the upper part of the cockpit, which justify the need to study the lower part as well. Figure 3.23 shows a zoom on the lower part of the duct.

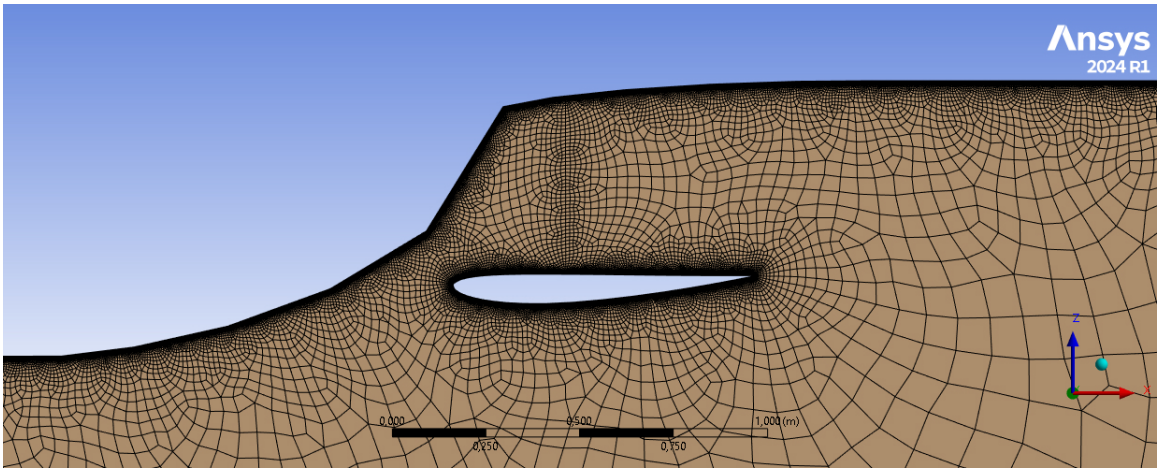

Figure 3.23 - *Zoom on the lower part of the mesh of the fluid domain in the two-dimensional model simulation.*

It can be observed in Fig. 3.23, that the mesh is refined at the place of the actuator disk and in the space between the duct and the cockpit. Even though the simulations will first be done without the AD, the same mesh will be used as it is still important to have a thin mesh inside of the duct in order to accurately capture the mass flow passing through the duct.

The same mesh quality analysis as for the axisymmetric mesh is performed. The number of elements and its characteristics are presented in Table 3.5.

Table 3.5 - *Characteristics of the elements of the mesh of the two-dimensional model simulation.*

Type of elements	quantity
TriShell3	409
QuadShell4	574491
Total	574900

It can be seen that the mesh is performed with mostly quad-element as the triangular elements only consist in 0.07 % of the mesh and with approximately two times more elements than in the half body case. The quality mesh will be analyzed as in the previous section, with Figure 3.24 for the aspect ratio, Figure 3.25 for the orthogonal quality and Figure 3.26 for the skewness of the elements of the mesh.

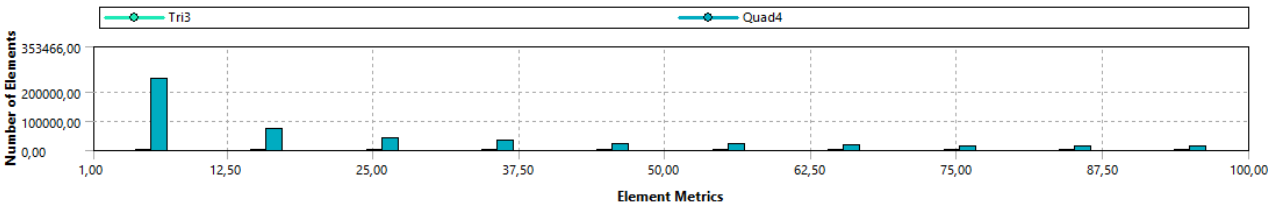

Figure 3.24 - *Distribution of the aspect ratio for triangular (Tri3) and quadrilateral (Quad4) mesh elements.*

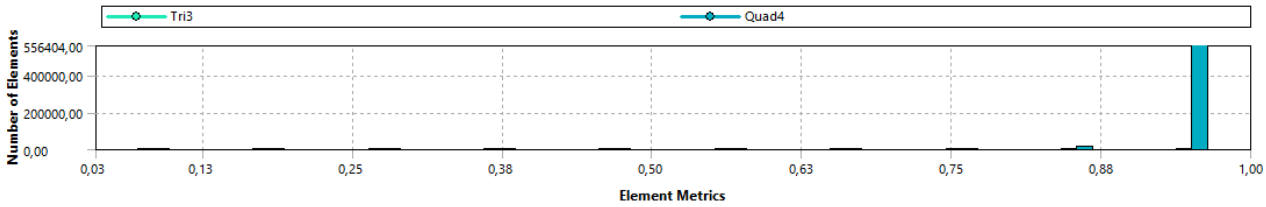

Figure 3.25 - *Distribution of the orthogonal quality for triangular (Tri3) and quadrilateral (Quad4) mesh elements.*

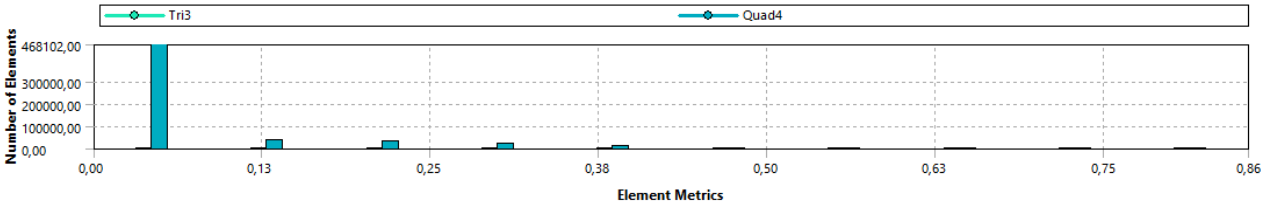

Figure 3.26 - *Distribution of the skewness for triangular (Tri3) and quadrilateral (Quad4) mesh elements.*

It can be observed from Fig. 3.24, Fig. 3.25 and Fig. 3.26 that the quality of this mesh is like the quality of the mesh of the axisymmetric simulation. It is not surprising as half of the mesh is similar to this case, however, those graphs allow to validate new part of the mesh (corresponding to the lower part) as well.

3.4.2 Results of the two-dimensional simulation

The results obtained in the two-dimensional simulation will be divided in two parts. First the velocity and pressure will be analyzed in cruise conditions (at the designed point) the turbulent intensity will also be shown. Then the inlet will be analyzed by looking at the velocity and mass flow on the upper part and on the down part. The force generated by the duct will also be studied.

The pressure-jump condition at the fan could not be put the same way as in the axisymmetric case, as the axial velocity is out of the theoretical range computed using the blade element method. As the objective of this section is not to validate the thrust generated nor look at the performance graphs but is to study the inlet and the velocity profiles, the pressure-jump condition is chosen to be the same in the upper and in the lower part of the fan. This delta pressure is set as 371 Pa, which corresponds to the designed point of the rotor.

Velocity and pressure analysis

The velocity magnitude obtained in cruise conditions for the two-dimensional model is shown in Fig. 3.27, the static pressure distribution in Fig. 3.28 and the turbulence intensity in Fig. 3.29.

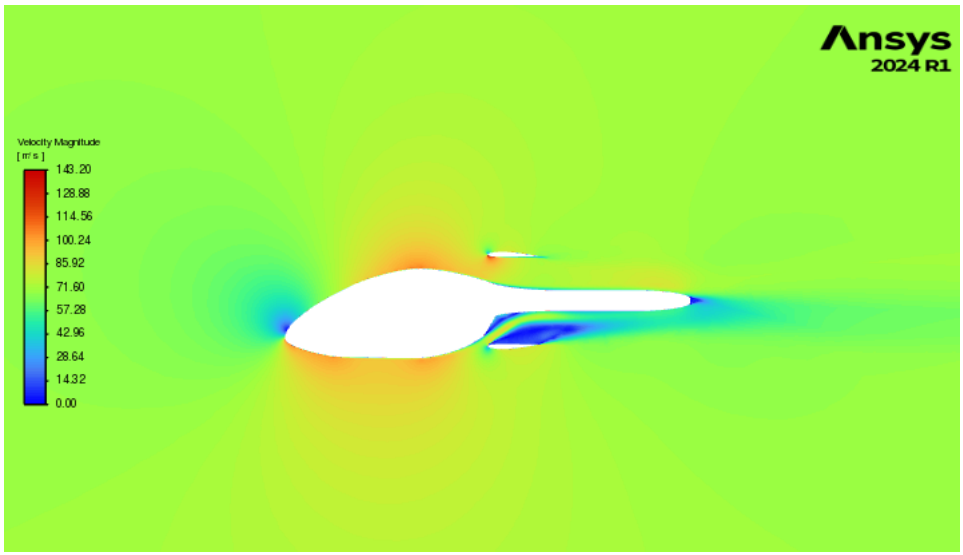

Figure 3.27 - *Velocity magnitude of the non-symmetrical two-dimensional model in cruise conditions.*

From Figure 3.27, it can directly be noticed that the location of interest will be the lower part of the ducted fan. Indeed, there is a high velocity variation where the rotor is placed in the lower part. This graph allows to see the location where the velocity magnitude is zero, as in the axisymmetric case, there is a stagnation point in the front of the cockpit and in the leading edge of the duct, but there are also other places where the velocity is zero. It can be observed that in the low right side of the cockpit, there is a triangle of stagnation fluid, and above the down part of the duct, there is a large zone with no velocity. The details of the decomposition in axial and radial velocity can be found in the Appendix B

but will not be detailed here as it does not add any information to the study.

The static pressure distribution can be observed in Figure 3.28

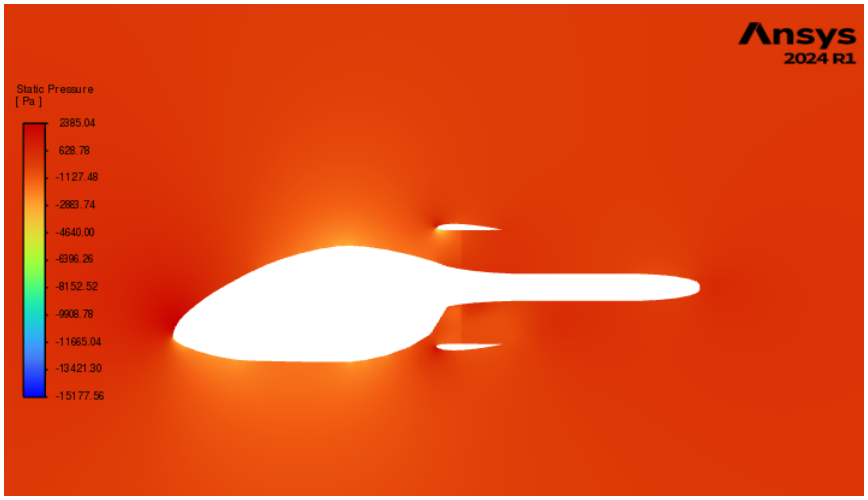

Figure 3.28 - *Static pressure distribution of the non-symmetrical two-dimensional model in cruise conditions.*

The two pressure-jump can be observed on the graph but can barely be seen, as the color range goes from 2365 Pa to -15177 Pa. Having a point where the static pressure is -15177 Pa is unrealistic, and as it is not a value that occurs at a lot of places, it is considered as a singular point. Having a singular point can come from several sources, as singularity in the mesh or in the geometry, it can be due to approximation round-off errors in the numerical method or convergence issues. As the objective is not to quantify exactly any variable but to see the tendency and the average or global behavior of the air around the airplane, this will not be further studied, but the precision of the results will be taken carefully.

The turbulent intensity can be seen in Figure 3.29.

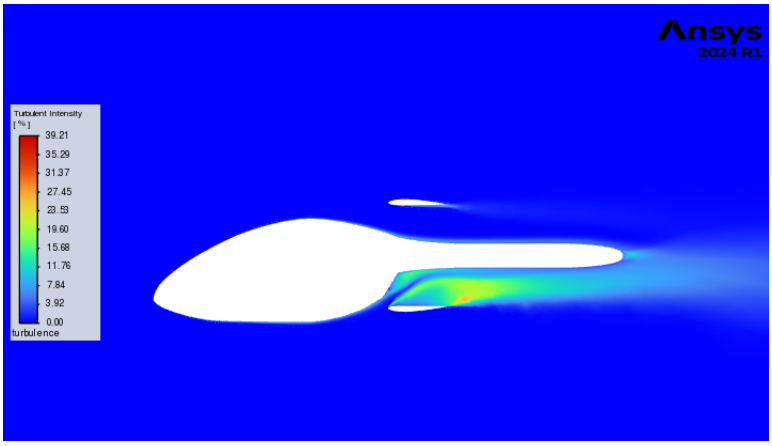

Figure 3.29 - *Turbulent intensity of the non-symmetrical two-dimensional model in cruise conditions.*

The turbulent intensity of the flow around the airplane allows to see that the flow is turbulent in the place where the lower part of the rotor is situated. Having turbulence in

the rotor can enhance several negative effects. Those aspects will be listed and explained hereafter.

- As the flow will highly diverge from the designed operating conditions and the inlet flow quality is decreased, a loss in the thrust efficiency of the rotor is engendered as the aerodynamic efficiency is reduced.
- As the turbulence occurs in the lower part only, a high distortion can be enhance, this phenomenon will be detailed in the next subsection.
- As a turbulent flow is not regular, unwanted phenomenon like vibration can be induced. Due to the difficulty to predict and describe precisely the turbulence, those phenomena are difficult to study.

Inlet velocity and duct generated forces

The objective of this last subsection was to detail the forces generated by the duct and the velocity inside of the duct. As the forces (the drag or the thrust) at the duct are computed using the integral of the pressure along the surface, the resulting force will not be analyzed in detail, due to the presence of singular points in the static pressure distribution. It can still be deduced from the previous analysis that the forces generated by the duct will be highly different in the upper and in the lower part. A more detailed analysis must be performed to study possibility of structural problems enhanced by this dis-balance.

Table 3.6 shows the velocity and mass flow inside of the duct at a position right before the rotor, each values is divided into its upper and lower component, corresponding to the component in the upper and lower part of the duct.

Table 3.6 - *Axial velocity and mass flow inside of the duct entering the rotor on the upper and lower part in the case with and without AD.*

	Velocity-x in [m/s]		Mass flow in [kg/s]	
	up	down	up	down
without AD	71.3	21.0	32.2	9.7
with AD	76.9	22.8	34.7	10.5

The values of the velocity and mass flow are computed as the average on the section in the lower and upper part of the interior of the duct, they allow to see the tendency of the flow but should not be taken as exact or precise values.

A difference in axial velocity between the upper and the lower part of the rotor can be noticed. The velocity and the mass flow below the fuselage has a magnitude which is 3 times lower than the velocity above the fuselage. Even though the difference might diverge from those values, due to the geometry of the lower inlet, it is probable that the velocity and mass flow will be highly different on the upper and lower part. In the reality, the change in velocity and mass flow will be progressive, as this simulation only shows a plan of the extreme case of inlet, but the obstruction occurs slowly around the cockpit. It can also be seen from Table 3.6 that the actuator disk has a suction effect, that increase the mass flow and the velocity at the rotor but without reducing the difference between the lower and upper part.

This difference in airflow conditions entering the duct or fan is called distortion and can lead to structural problems for the blades. As the blades rotate, inlet obstruction causes them to be periodically subjected to varying forces, increasing vibration and fatigue. Additionally, rotor distortion leads to a loss in stall margin, which is the difference between the fan's operating point and the point at which aerodynamics stall occurs [21] [36]. A three-dimensional study is essential to analyze global distortion, considering the entire duct inlet and not only the differences between the upper and lower cockpit regions.

3.5 Conclusion

In this chapter, the CFD study was performed, modeling the rotor with an actuator disk. First, the mesh was analyzed with four quality criteria. Then, an axisymmetric model was simulated, focusing on velocity and pressure distribution along the cockpit during cruise. The duct's contribution to thrust was also analyzed, showing that it added 4.5 % to the total thrust at the cruise design point. The performance charts highlighted differences between flight and axial velocity. The thrust contribution of the duct is studied varying with flight speed.

Then a two-dimensional model was simulated, to study the integration of the duct with the cockpit. It revealed zones of zero velocity and high turbulence inside the duct, particularly in the lower cockpit, leading to potential engine distortion that will have to be studied in more details in further analyses.

Chapter 4

Conclusion

The objective of this thesis was to study the ULM Mindus Belvedere using a computational fluid dynamic study focusing on the ducted fan engine placed at the rear of the cockpit. To do so, the design of the rotor and the stator had to be performed in more details as the information already computed in a previous preliminary design were not sufficient to perform the CFD study straightforward. After the design, the CFD study was carried out at cruise, restricted to the front part of the airplane and some additional geometry hypotheses were made.

First the design of the rotor and the stator was performed. To do so, the blade element method has been adapted in a design way. Using this method and adapting it to a ducted fan, the velocity triangle and thus the generated forces could be computed. With an estimation on the axial velocity inside of the duct and the required thrust, an estimation of the losses has been computed and the required work could be obtained. The required rotor- and stator chord and stagger angle to generate the thrust were computed for two airfoils, the NACA 2412 and the NACA 65-210. After analysis of the two designs, the NACA 65-210 was chosen.

After, the performance analysis of the design was made. To do so, the thrust and power coefficients as well as the propulsive efficiency varying with the advance ratio were computed using a BEM method. The software DFDC, which is adapted for ducted fan, was used to confirm the performances of the designed rotor. In both analyses, the value global efficiency was computed as over 0.8.

Then, a computational fluid dynamic study was performed using an actuator disk to simulate the rotor, first in axisymmetry and then in two dimensions. The axisymmetric simulation allowed us to study the velocity and the pressure distributions along the cockpit, as well as the forces at the duct. It was observed that the duct was adding 4.5 % to the thrust generated by the rotor, at the designed point. Varying the flight velocity, the performance charts could be reproduced, considering a more realistic axial velocity than in the previous chapter. The difference between the flight velocity and the axial velocity could be observed in more details, varying with the flight velocity. It was seen that this difference was mostly positive at low collective pitch angle and low flight speed. Then the thrust coefficient could be analyzed considering the duct. It was observed that, when considering the contribution to thrust of the duct, the ULM was generating more thrust at low flight velocity and less thrust at higher speed.

The two-dimensional analysis allowed to study in more details the integration of the

duct with the cockpit. The velocity magnitude and the pressure distributions around the cockpit could be analyzed. It was seen that the lower part of the cockpit was engendering zero-magnitude velocity zones and a high turbulence intensity inside of the duct. The details of the velocity and mass flow going through the upper and lower part of the cockpit showed highly different behaviors which could engender distortion in the engine.

4.1 Outlook for future research

As shown in this work, the design of the rotor and the stator of the ducted fan was efficient, with each component fulfilling its role, but this remains a preliminary design. Some improvements could be made to improve the efficiency of the DFS. For example, in this work, only one airfoil was used for both the stator and rotor across all radial stations. In practice, using two airfoils would be preferred: a thicker and more robust airfoil at the hub, capable of handling higher loads and providing structural strength, and a thinner, more aerodynamic airfoil at the tip to reduce drag and improve efficiency at lower loads. Furthermore, optimizing the work distribution along the span could improve efficiency by putting more work to regions where thrust is generated more effectively.

To continue the aircraft study, a full 3D CFD analysis of the entire plane will be required, this will help to focus particularly on the rotor's effect on the tail. Even though the swirl induced in the air flow is already diminished by the stator, a more detailed CFD study will permit a precise understanding of what is truly happening and the other consequences that could be engendered on the tail, having the DFS at the back of the ULM. Additionally, a total three-dimensional CFD simulation will help to examine the airflow entering the duct in all regions, not just above and below but across the entire inlet area.

As could be seen in the last part of this work, the geometry of the lower part of the cockpit will engender turbulence and probably distortion in the inlet of the ducted fan. To avoid that, the lower part of the cockpit's geometry could be reviewed and made more aerodynamically to avoid those negative aspects. Another idea could be to put the duct a bit closer to the end of the ULM, but this could lead to troubles at the V-Tail as previously mentioned, it could even be put at the rear of the aircraft, like the Faradair [12]. Further analyses must be made to verify and ameliorate the ducted fan system.

Appendix A

Characteristics of the airfoils

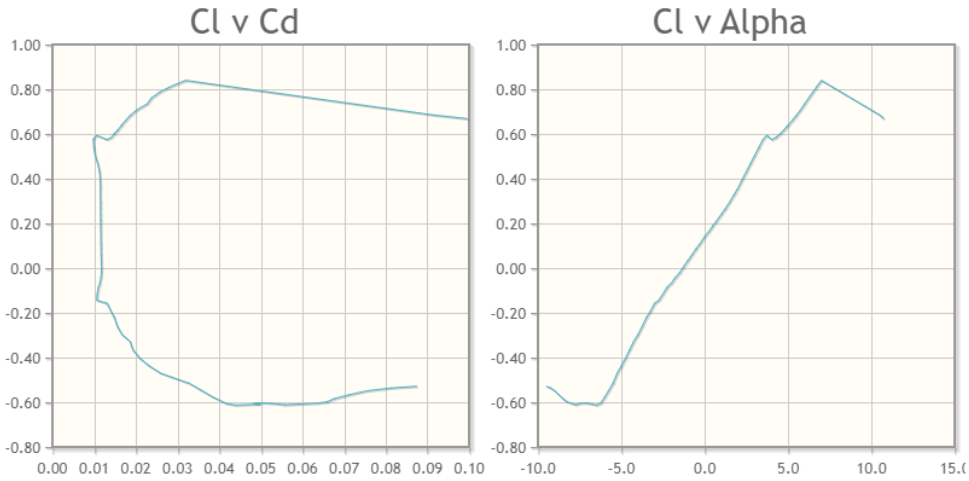

Figure A.1 - *Polars of the NACA 65-210 obtained with XFOIL.*

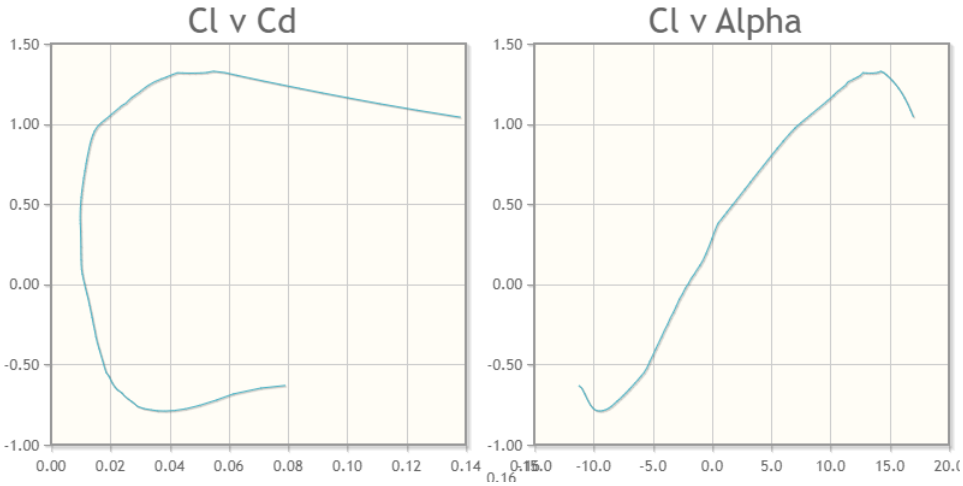

Figure A.2 - *Polars of the NACA 2412 obtained with XFOIL.*

Appendix B

Two-dimensional simulation axial and radial velocities

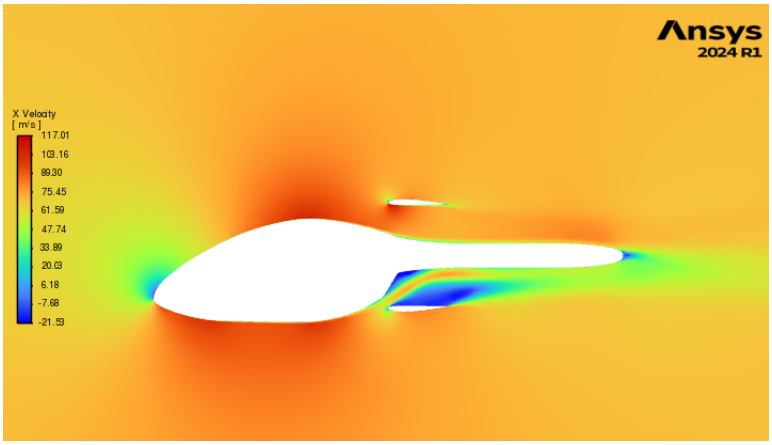

Figure B.1 - *Velocity along x of the two-dimensional model in cruise conditions.*

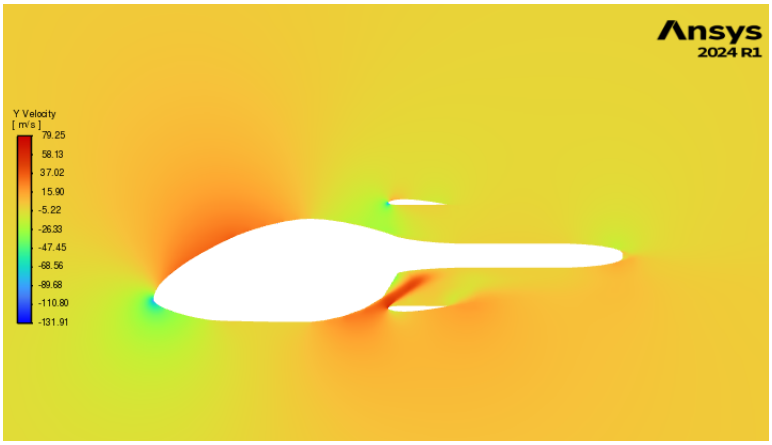

Figure B.2 - *Velocity along y of the two-dimensional model in cruise conditions.*

Bibliography

[1] University archives photograph collection - xaz-1 marvelette. [Online; accessed April 2024].

[2] Ira H. Abbott, Albert E. Von Doenhoff, and Jr. Stivers, Louis. Summary of airfoil data. 1945. [Online; accessed May 2024].

[3] Absolute Pilots. How the naca 2412 aerofoil saves you €, 2022. [Online; accessed March 2024].

[4] Ansys Inc. *Ansys Fluent*, 2024. Version 2024, Fluid Simulation Software.

[5] ANSYS, Inc. *ANSYS Fluent User's Guide, PART II: MESHING MODE*, 2024. Accessed: 2024-07-12.

[6] Fanjet Aviation. The aircraft - fan jet 600. [Online; accessed April 2024].

[7] D.M. Black, H.S. Wainauski, and C. Rohrback. Shrouded propellers - a comprehensive performance study. 1968. Presented at the 5th AIAA Annual Meeting and Technical Display.

[8] N. Cumpsty. *Compressor Aerodynamics*. Longman, Harlow, England, 2nd edition, 2004.

[9] Dan Johnson. Flying Germany's Longtime Leader, the Affordable Comco Ikarus C42. [Online; accessed March, 2024].

[10] European Union. Sustainable Development Goals: Goal 12. `https://www.undp.org/european-union/sustainable-development-goals`. [Online; accessed March, 2024].

[11] European Union. Regulation (EU) 2018/1139 of the European Parliament and of the Council of 4 July 2018 on common rules in the field of civil aviation and establishing a European Union Aviation Safety Agency. `https://eur-lex.europa.eu/legal-content/EN/TXT/?uri=CELEX%3A32018R1139`, 2018. [Online; accessed August, 2024].

[12] Faradair Aerospace. Faradair: Sustainable aviation solutions. `https://www.faradair.com/`. [Online; accessed August 2024].

[13] Fliegermagazin. C42 C Technical data. `https://www.comco-ikarus.de/c42-c-en/?lang=en`. [Online; accessed March, 2024].

[14] Fliegermagazin. UL-Pilot-Report: Comco Ikarus C42 C. `https://www.fliegermagazin.de/flugzeuge/ul-pilot-report-comco-ikarus-c42-c/`. [Online; accessed March, 2024].

[15] Oleson RPatrick H. Small aircraft propeller noise with ducted propeller. 1998.

[16] Schlichting Hermann and Gersten Klaus. *Boundary-Layer Theory*. Springer, 2017.

[17] Koen Hillewaert. Aerospace propulsion (aero0014), 2023. Département Aérospatiale et Mécanique, Design of Turbomachines (DoT), Academic year 2022-2023.

[18] Charles Hirsch. *Numerical Computation of Internal and External Flows*. Butterworth-Heinemann, Oxford, 2nd edition, 2007.

[19] Historic Wings. Stipa-Caproni: The Flying Barrel. [Online; accessed April 2024].

[20] Milton M. Kelin. Pressure distributions and force tests of an naca 65-210 airfoil section with a 50-percent-chord flap. 1947. [Online; accessed March 2024].

[21] K. B. Lee, M. Wilson, and M. Vahdati. Effects of inlet disturbances on fan stability. *Journal of Engineering for Gas Turbines and Power*, 141(5):051014, 2019.

[22] Peiqing Liu. *Aerodynamics*. Springer Singapore, 2022.

[23] M. Drela, H. Youngren. *Ducted Fan Design Code (DFDC) - Axisymmetric Analysis and Design of Ducted Rotors, Tech. Rep.*, 2005. [Online; accessed March, 2024].

[24] John E. Matsson, Aaron Voth, Mark McCain, and Mason McGraw. Aerodynamic performance of the naca 2412 airfoil at low reynolds number. 2020. [Online; accessed March 2024].

[25] N. McCarthy. The most produced aircraft of all-time. `https://www.statista.com/chart/20788/aircraft-models-with-the-highest-estimated-production-figures/`, 2021. [Online; accessed April, 2024].

[26] Florian R. Menter. *Two-Equation Eddy-Viscosity Turbulence Models for Engineering Applications*, volume 32. 1994.

[27] F. Marc De Piolenc and Goerge E. Wright Jr. *Ducted Fan Design- volume 1- propulsion physics and design of fans and long-chord ducts*. 2001.

[28] D.P. Raymer. *Aircraft design: a conceptual approach*. 2004.

[29] M. Bakhsheshizanjani1 A. Khoshnejad1 A. Doostmahmoudi. S. G. Pouryoussefi1, G. Abdolali1. Experimental investigation of aerodynamic characteristics of an embedded wing-electric ducted fan boundary layer ingestion setup. June 2022.

[30] A H Sack8 and J A Burnell. *DUCTED PROPELLERS-A CRITICAL REVIEW OF THE STATE OF THE ART*. 1962.

[31] Vincent Terrapon. Computational fluid dynamics. Course lecture, 2023.

[32] N.H.M. van den Dungen. Synthesis of an aircraft featuring a ducted-fan propulsive empennage. Master's thesis, 2017.

[33] Frank M. White. *Fluid Mechanics*. McGraw-Hill, New York, 5th edition, 2003.

[34] Wikipedia. Bell X-22. `https://upload.wikimedia.org/wikipedia/commons/4/44/X-22a_onground_bw.jpg`. [Online; accessed March, 2024].

[35] David C. Wilcox. *Turbulence Modeling for CFD.* DCW Industries, La Canada, CA, 3rd edition, 2006.

[36] W. Zhang, S. Stapelfeldt, and M. Vahdati. Influence of the inlet distortion on fan stall margin at different rotational speeds. *Aerospace Science and Technology*, 98:105668, 2020.